International Journal of Plasticity 158 (2022) 103417

Contents lists available at ScienceDirect

International Journal of Plasticity

journal homepage: www.elsevier.com/locate/ijplas

Mechanical behaviors of equiatomic and near-equiatomic face-centered-cubic phase high-entropy alloys probed using *in situ* neutron diffraction

Daixiu Wei [a,*], Wu Gong [b], Tomohito Tsuru [c,d,e], Takuro Kawasaki [b], Stefanus Harjo [b], Biao Cai [f], Peter K. Liaw [g], Hidemi Kato [a]

[a] Institute for Materials Research, Tohoku University, 2-1-1 Katahira, Sendai, Miyagi, 980-8577, Japan
[b] J-PARC Center, Japan Atomic Energy Agency, 2-4, Shirakata, Tokai, Naka-gun, Ibaraki, 319-1195, Japan
[c] Nuclear Science and Engineering Center, Japan Atomic Energy Agency, 2-4 Shirakata, Tokai-mura, Ibaraki, 319-1195, Japan
[d] Elements Strategy Initiative for Structural Materials, Kyoto University, Yoshida-honmachi, Sakyo-ku, Kyoto, 606-8501, Japan
[e] PRESTO, Japan Science and Technology Agency, 4-1-8 Honcho, Kawaguchi, Saitama, 332-0012, Japan
[f] School of Metallurgy and Materials, University of Birmingham, Edgbaston, Birmingham, B15 2TT, United Kingdom
[g] Department of Materials Science and Engineering, The University of Tennessee, Knoxville, TN, 37996, USA

ARTICLE INFO

Keywords:
High-entropy alloy
Stacking fault energy
Mechanical property
Plasticity
Mechanical twinning
Martensitic transformation

ABSTRACT

The equiatomic CoCrFeMnNi Cantor alloy, a face-centered-cubic (FCC) single-phase high-entropy alloy (HEA), has attracted considerable attention owing to its high strength and good ductility over a wide temperature range. The mechanical performance of this alloy was improved by reducing the stacking fault energy (SFE) through composition modification, and thus, a series of near- or non-equiatomic HEAs that are stronger and more ductile than their predecessor have been developed. However, the plastic-deformation behavior and strengthening mechanisms have not yet been fully discovered. In this study, we investigated the yielding and hardening behaviors of the Cantor alloy and FCC-phase Co-rich HEAs with different SFEs by *in situ* neutron diffraction combined with the first-principles method and electron-microscopy characterizations. The Co-rich HEAs exhibited a higher intrinsic yield strength than the Cantor alloy, mainly because of the larger shear modulus or modulus misfit, and grain refinement being more effective in improving the yield strength of low-SFE HEAs. Furthermore, higher flow stresses and better ductility of the Co-rich HEAs are attributed to the greater dislocation density and a larger number of stacking faults, which enhanced the strain-hardening rate during tensile deformation. The low SFE promoted mechanical twinning, and martensitic transformation contributed to higher strain-hardening rates. The present study provides deep insight into the yielding and hardening of FCC-phase HEAs, the understanding of which is a prerequisite for developing high-performance materials.

1. Introduction

Metals and alloys are irreplaceable structural materials used in a wide variety of applications. Conventional alloys are designed

* Corresponding author.
E-mail address: wei1987xiu@imr.tohoku.ac.jp (D. Wei).

https://doi.org/10.1016/j.ijplas.2022.103417
Received 30 June 2022; Received in revised form 20 August 2022;
Available online 7 September 2022
0749-6419/© 2022 The Author(s). Published by Elsevier Ltd. This is an open access article under the CC BY-NC-ND license (http://creativecommons.org/licenses/by-nc-nd/4.0/).

based on one principal element with minor additions of alloying elements to enhance the mechanical properties by solid solution strengthening, grain boundary strengthening, and precipitation strengthening (Beer, Johnston Jr. Dewolf, 2006; Reza Abbaschian, Lara Abbaschian and Reed-Hill, 2009). For instance, steels are Fe-based alloys with minor additions of Mn, Ni, Cr, C, etc. In the year 2004, a different concept was proposed, in which the alloy design is based on five or more principal elements with equimolar or near-equimolar proportions (Cantor et al., 2004; Yeh et al., 2004). These alloys are known as multi-principal alloys or high-entropy alloys (HEAs) (Cantor et al., 2004; Miracle and Senkov, 2017; Tsai and Yeh, 2014; Yeh et al., 2004; Zhang et al., 2014). Subsequently, face-centered-cubic (FCC) phase HEAs such as CoCrFeMnNi Cantor alloy, hexagonal closed-packed (HCP) phase HEAs such as GdHoLaTbY alloy, and body-centered-cubic single-phase HEAs such as TiZrHfNbTa Senkov alloy, have been successfully developed (Cantor et al., 2004; Gao et al., 2015; Miracle and Senkov, 2017; Senkov et al., 2010; Tsai and Yeh, 2014; Zhang et al., 2014). Soon afterwards, medium entropy alloys (MEAs) composed of three or four multi-principal elements also emerged. The FCC-phase CoCrFeMnNi, CoCrFeNi, and CoCrNi alloys are the most widely investigated HEAs/MEAs; which possess a good combination of strength and ductility, particularly at low temperatures, making it a promising candidate for cryogenic applications (Cantor et al., 2004; Gali and George, 2013; Gludovatz et al., 2014; Laplanche et al., 2016; Li et al., 2022, 2022; Otto et al., 2013; Schneider et al., 2020). The three HEAs/MEAs have a medium stacking fault energy (SFE) of 18 to 27 mJ/m^2 at ambient temperature (Liu et al., 2018), but the SFE decreases with a decrease in temperature (Huang et al., 2015). Mechanical twinning occurs during deformation and is preferred at lower SFE. Mechanical twinning contributes to the strengthening and ductilization of the alloys (Kaushik et al., 2021; Li et al., 2022, 2022), which is known as the twinning-induced plasticity (TWIP) effect (De Cooman et al., 2018).

In FCC-phase metals and alloys, the SFE is the major factor determining the plasticity mechanism and mechanical properties. During plastic deformation, the gliding of perfect dislocations with a Burgers vector of a/2 <110> and the formation of dislocation-cell structures have been widely observed in metals with a high SFE (higher than 45 mJ/m^2), such as pure Ni and Al (Carter and Holmes, 1977; Hammert et al., 1992; Richard W. Hertzberg, Richard P. Vinci, 2013). However, the dissociation of perfect dislocations into Shockley partial dislocations with a Burgers vector of a/6 <211> is often activated by the externally-applied shear stress in alloys with a medium SFE (usually 15 − 45 mJ/m^2), such as TWIP steels (De Cooman et al., 2018; Grässel and Frommeyer, 1998). In addition, mechanical twinning is often activated by the shear stress-aided overlapping of stacking faults (SFs) on constitutive {111} planes (De Cooman et al., 2018). These alloys often exhibit a high strain-hardening rate, which postpones the initiation of necking and thus, results in high strength and good ductility owing to the TWIP effect (He et al., 2022; Huang et al., 2019; Y. Z. Li et al., 2022; Zhang et al., 2020). Furthermore, in alloys with extremely low SFE (usually lower than 15 mJ/m^2), such as Co–Cr–Mo alloys (Pineau and Matdriaux, 1976; Wei et al., 2019a), the dissociation of perfect dislocations into Shockley partials becomes more preferred, and the strain-induced FCC → HCP martensitic transformation often occurs, in which the HCP phase is formed by overlapping SFs on every second {111} plane of the FCC matrix (Olson and Cohen, 1976). It also contributes to the increases in strength and ductility (Bahramyan et al., 2020; Connolly et al., 2022; Fang et al., 2019; Homayounfard and Ganjiani, 2022; Kim et al., 2022; Lai et al., 2022), known as the transformation-induced plasticity (TRIP) effect (Connolly et al., 2022; Fischer et al., 2000).

To date, numerous strategies have been utilized for further improving the strength of the HEAs/MEAs, such as grain refinement (Agius et al., 2022), precipitation strengthening (F. He et al., 2021; Liu et al., 2022; Ye et al., 2022), dislocation cell strengthening (He et al., 2022; Y.Z. Li et al., 2022), gradient nanostructure strengthening (Sun et al., 2022), interstitial strengthening (Z. He et al., 2021; Zhang et al., 2022), chemical fluctuation strengthening (Z. He et al., 2021; Wei et al., 2022c; Zhang et al., 2021), and TWIP/TRIP strengthening (Bahramyan et al., 2020; Lai et al., 2022; Wei et al., 2022a, 2022b; Zhang et al., 2020). Hereinto, significant efforts have been devoted to developing strong and ductile FCC-phase HEAs by further reducing the SFE of the CoCrFeMnNi HEA achieved by modifying the composition, and many types of non-equiatomic single-phase TWIP/TRIP HEAs have been designed (Deng et al., 2015; Li et al., 2016; Wei et al., 2019b, 2019c, 2019d). For instance, Co-rich HEAs exhibit higher strength and better ductility than equimolar CoCrFeMnNi alloys (Wei et al., 2019b, 2019c, 2019d). However, the reason for the high yield strength of Co-rich HEAs is unclear. The mechanisms of plasticity and dynamic strengthening, as well as microstructural evolution under plastic deformation, have not been investigated. At the same time, grain refinement is an effective strategy to improve the yield strength by grain-boundary strengthening (Hall–Petch relationship) (Hall, 1951; Petch, 1953), where the grain size affects not only the yield but also the strain-hardening behavior. The Hall–Petch relationship is determined by the intrinsic properties of alloys. It has been reported that the intrinsic friction stresses and the Hall–Petch coefficients of equiatomic CoCrNi and CoCrFeMnNi alloys are higher than those of pure metals (Yoshida et al., 2019, 2017). Thus, grain refinement facilitates the effective strength improvement in these alloys. However, the effect of the grain size on the yielding and the strengthening mechanisms of the Co-rich HEAs has not been clarified, where a good understanding of them is a prerequisite for optimizing the microstructures and mechanical properties.

In this study, we aimed to demonstrate the yielding and strengthening behaviors of three representative HEAs: equiatomic $Co_{20}Cr_{20}Fe_{20}Mn_{20}Ni_{20}$ (atomic percent, at.%) Cantor HEA, Co-rich $Co_{35}Cr_{20}Mn_{15}Ni_{15}Fe_{15}$ TWIP-HEA (Wei et al., 2019c), and Co-rich $Co_{35}Cr_{25}Mn_{15}Ni_{15}Fe_{10}$ TRIP-HEA (Wei et al., 2019c). The effects of intrinsic properties and grain sizes on room-temperature mechanical performance were investigated and discussed, based on experiments and first-principles calculations. The dynamic plastic-deformation behavior, strain-hardening mechanism, and microstructure evolution during tensile deformation were clarified by *in situ* neutron diffraction (ND) measurements. The results obtained deepen the understanding of strengthening in HEAs, contributing to the design and fabrication of high-performance HEAs for load-bearing applications.

2. Methodology

2.1. Sample preparation and experimental investigations

Ingots of $Co_{20}Cr_{20}Mn_{20}Ni_{20}Fe_{20}$, $Co_{35}Cr_{20}Mn_{15}Ni_{15}Fe_{15}$, and $Co_{35}Cr_{25}Mn_{15}Ni_{15}Fe_{10}$ HEAs were prepared via high-frequency induction melting and vacuum casting. The weight of each ingot is 700 g, which has a thickness of 20 mm and a width of 50 mm. Hereafter, the samples are denoted as Fe_{20}, Fe_{15}, and Fe_{10}, respectively. The cast ingots were homogenized at 1473 K for 5 h in a high-purity Ar atmosphere and then forged to a 50% reduction in thickness at 1473 K with water quenching to 293 K. After that, the samples were cold-rolled to a 40% reduction in thickness at 293 K. Finally, pieces were sliced from the cold-rolled sheet and annealed at 1173, 1273, 1373, and 1473 K for 2.4×10^2 s, 6.0×10^2 s, 1.8×10^3 s, 3.6×10^3 s, 2.16×10^4 s, 4.32×10^4 s, 8.64×10^4 s, 2.592×10^5 s, and 4.32×10^5 s. After annealing, recrystallized grain structures with different grain sizes were formed.

Then, dog-bone-shaped tensile samples with gauge dimensions of $6.4 \times 2.5 \times 1.5$ mm were sliced, and the sample surfaces were polished, using abrasive papers up to 2000 grit. Uniaxial tensile tests were conducted at 293 K and a strain rate of 1×10^{-3} s^{-1}, employing a Shimadzu AG-50kNX test frame. The strain was calibrated, using a video extensometer. The grains were characterized, utilizing scanning electron microscopy (JSM-7100F, JEOL) equipped with electron backscatter diffraction (EBSD). The acquired data were analyzed, using the OIM software (version 7.0). A grain tolerance angle of 5° was used to identify the grain boundary (Beausir et al., 2009; Raju et al., 2008), because the average grain size determined using the OIM for a tolerance angle of 5° is in good agreement with the grain size measured using the TEM (Raju et al., 2008). The boundary with a misorientation angle of 2 – 5° was considered as the subgrain boundary. The annealing twin boundaries were included as the identified grain boundaries. The mean grain size was calculated by weighting the area of each grain as follows:

$$\bar{\nu} = \frac{\sum_{i=1}^{N} A_i \nu_i}{\sum_{i=1}^{N} A_i} \tag{1}$$

where A_i is the area of grain i.

In situ tensile deformation experiments combined with ND measurements of the HEAs were conducted, using a time-of-flight neutron diffractometer at BL19 "TAKUMI" in the Materials and Life Science Facility at the Japan Proton Accelerator Research Complex. The details of the diffraction instrument are described in a previous study (Harjo et al., 2011). As illustrated in Fig. 1, the loading axis was oriented at +45°, relative to the incident neutron beam. Axial and radial detectors were used to collect the diffracted neutrons, which provided the microstructure characteristics of the bulk samples along the tensile direction and normal direction, respectively. To clarify the correlation between the microstructure evolution and flow stress, the ND profiles collected by the axial detector were used for the line profile analysis in the present study. The covered d-range was 0.05 – 0.30 nm with an instrumental peak resolution ($\Delta d/d$) of 0.3%. For the ND line profile analysis, the lattice parameter and {hkl}-dependent d-spacing were analyzed, utilizing the Z-Rietveld software (Oishi-Tomiyasu et al., 2012; Oishi et al., 2009). The dislocation density was calculated, employing the convolutional multiple whole profile (CMWP) method, where the diffraction profiles (I^{hkl}) are expressed as (Ribárik et al., 2020, 2001; Ungár et al., 2010):

$$I^{hkl} = I^{hkl}_{instr} * I^{hkl}_{size} * I^{hkl}_{disl} * I^{hkl}_{planar} \tag{2}$$

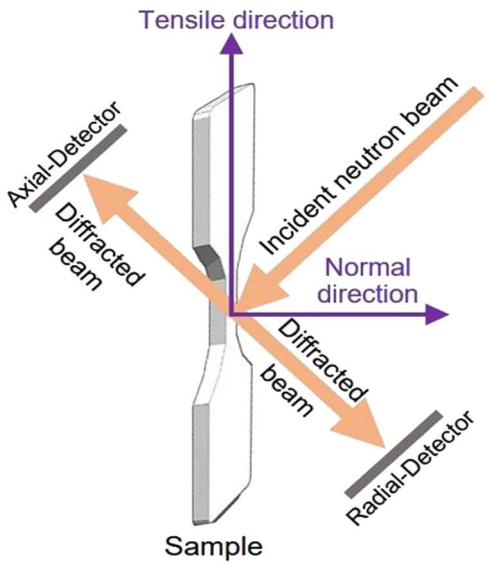

Fig. 1. Illustration of *in-situ* neutron diffraction measurement for the HEAs.

where I_{instr}^{hkl} is the measured instrumental profile, I_{size}^{hkl} is the size profile, I_{disl}^{hkl} is the strain profile of dislocations, and I_{planar}^{hkl} is the profile function of planar faults. Here, the strain Fourier transform ($A^D(L)$) is (Gubicza, 2014; Ungár et al., 2001; Wilkens, 1970):

$$A^D(L) = \exp\left[-\frac{\pi b^2}{2}\left(g^2\overline{C}\rho_d L^2 f\left(\frac{L}{R_e^*}\right)\right)\right] \tag{3}$$

$\overline{C}$ is the average dislocation contrast factor, ρ_d is the dislocation density, b is the Burgers vector of dislocations, L is the Fourier length, f is the Wilkens function, and R_e^* is the effective cut-off radius of the dislocations. The value of $\overline{C}$ is calculated as (Gubicza, 2014; Ungár et al., 2001; Wilkens, 1970):

$$\overline{C} = \overline{C_{h00}}\left(1 - q\frac{h^2k^2 + k^2l^2 + l^2h^2}{\left(h^2 + k^2 + l^2\right)^2}\right) \tag{4}$$

q is a parameter describing the dislocation character, $\overline{C_{h00}}$ is the average contrast factor of the $(h00)$ reflection, which is calculated, using the ANIZC software (Borbély et al., 2003). The elastic constants of the HEAs listed in Table 1 were obtained from first-principles calculations. The instrumental profile for CMWP analysis was obtained by measuring the National Institute of Standards and Technology Standard Reference Material 660a LaB6 standard powder (NIST, 2000). The substructures of the deformed HEAs were observed, using transmission electron microscopy (TEM, JEM-2000EXII, JEOL) at a voltage of 200 kV. The TEM specimens were prepared, using an ion-milling system (PIPS II Model 695, Gatan) with a milling angle of 4° and an ion beam energy of 3.0 kV. The shear modulus of the bulk polycrystalline samples were measured using a sing-around measurement technique (Ultrasonic Engineering UVM-2).

2.2. First-principles calculations

To interpret our experimental results based on established mechanisms and concepts for HEA strengthening, material properties that cannot be measured experimentally were necessary. Thus, the first-principles electronic structure calculations were employed. Atomic models of 180–atom supercell with dimensions of $\mathbf{a} = 5\mathbf{e}_1$, $\mathbf{b} = 3\mathbf{e}_2$, and $\mathbf{c} = 2\mathbf{e}_3$ ($\mathbf{e}_1 = a_0[\sqrt{2}/2,0,0]$, $\mathbf{e}_2 = a_0[0,\sqrt{6}/2,0]$, and $\mathbf{e}_3 = a_0[0,0,\sqrt{3}]$, where a_0 is the lattice constant) and a coordinate system corresponding to $x = [1\bar{1}0]$, $y = [11\bar{2}]$, and $z = [111]$ were constructed for the considered HEAs. Special quasi-random structures (SQS) were generated using the "mcsqs" function in the Alloy Theoretic automated toolkit (ATAT) to model statistically random solid HEA solutions (Van de Walle et al., 2002). We carried out the first-principles calculations within the framework of density functional theory (DFT) using the Vienna *Ab initio* Simulation Package (Kresse and Furthmüller, 1996; Kresse and Hafner, 1993), and projector-augmented wave potentials were employed with the Perdew–Burke–Ernzerhof generalized gradient approximation exchange-correlation density functional (Kresse and Joubert, 1999; Perdew et al., 1996). We selected the Brillouin-zone gamma-centered k-point samplings using the Monkhorst–Pack algorithm (Hu et al., 2019), in which $3 \times 3 \times 3$ grids were used for the 180–atom models. A cut-off of 400 eV in plane-wave energy was applied using a first-order Methfessel–Paxton scheme. The total energy converged within 10^{-5} eV/atom. The relaxed configurations were obtained using the conjugate gradient method, which terminated the search when the force on all the atoms was reduced to 0.01 eV/Å.

3. Results

Fig. 2 shows the average grain sizes of the Fe_{20} (Fig. 2a), Fe_{15} (Fig. 2b), and Fe_{10} (Fig. 2c) HEAs after annealing. It can be seen that the grain size increases with annealing temperature and annealing time. The grains grew more rapidly at higher temperatures than at lower temperatures. Furthermore, the grains of the Fe_{20} HEA tended to grow more rapidly than those of the Fe_{15} and Fe_{10} HEAs at 1473 K. The finest grain sizes obtained in the present study, 6.2 μm (Fe_{20}), 5.9 μm (Fe_{15}), and 5.7 μm (Fe_{10}), were obtained by annealing at 1173 K for 2.4×10^2 s, while the corresponding largest grain sizes, 292, 211, and 205 μm, in the three HEAs, were obtained by annealing at 1473 K for 4.32×10^5 s.

The EBSD IPF maps in Fig. 3 show the grain morphologies of the (Fig. 3a,d) Fe_{20}, (Fig. 3b,e) Fe_{15}, and (Fig. 3c,f) Fe_{10} HEAs after annealing at 1173 K for 2.4×10^2 s (Fig. 3a–c) and at 1373 K for 3.6×10^3 s (Fig. 3d–f). A relatively-homogeneous grain structure formed in all samples. The average grain sizes are approximately 6 μm (Fig. 3a–c), 77.3 μm (Fig. 3d), 73.8 μm (Fig. 3e), and 70.6 μm (Fig. 3f). The difference in the grain morphologies between Fig. 3a–f is that annealing twins are more frequently observed in Fig. 3d–f, which is correlated with the low SFE of the HEAs. The samples shown in Fig. 3a-c were utilized for *in situ* ND measurements and TEM

Table 1
Elastic modulus (E_{hkl}) along the {hkl} crystal orientation, lattice parameter (a_0), Burgers vector (b) of perfect dislocations, and the intrinsic stacking fault energy (γ_{isf}) of the Fe_{20}, Fe_{15}, and Fe_{10} HEAs, acquired from the *in-situ* ND line profile analysis.

Sample	E_{111} (GPa)	E_{200} (GPa)	E_{220} (GPa)	E_{311} (GPa)	a_0 (nm)	b (nm)	γ_{isf}
Fe_{20}	252.8	138.1	231.5	183.7	0.3598	0.2537	26.5±4.5
Fe_{15}	280.9	156.6	272.4	210.4	0.3583	0.2533	11.6±0.4
Fe_{10}	294.1	166.8	290.7	219.3	0.3585	0.2534	7.8±0.5

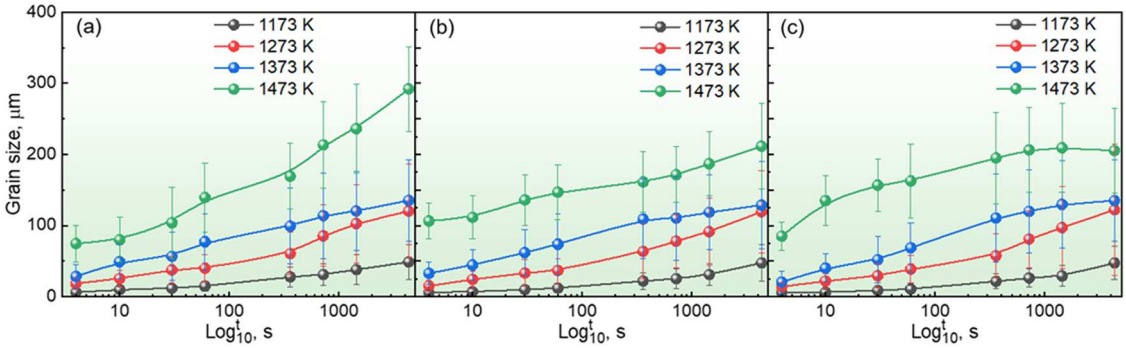

Fig. 2. Average grain size of the (a) Fe_{20}, (b) Fe_{15}, and (c) Fe_{10} HEAs after annealing at 1173 K, 1273 K, 1373 K, and 1473 K for a annealing time (t) of 2.4×10^2 s, 6.0×10^2 s, 1.8×10^3 s, 3.6×10^3 s, 2.16×10^4 s, 4.32×10^4 s, 8.64×10^4 s, 2.592×10^5 s, 4.32×10^5 s. The grain size was measured by EBSD method.

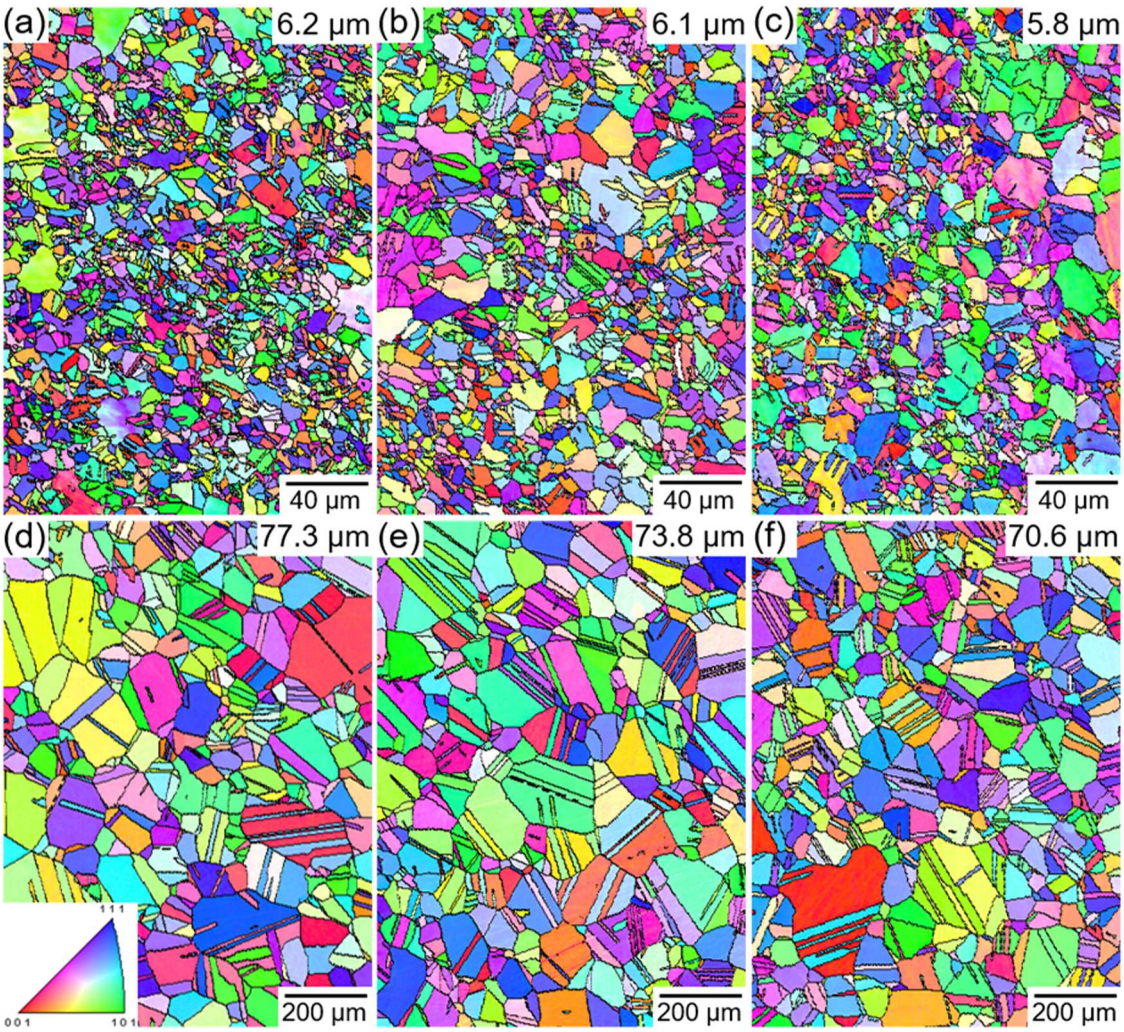

Fig. 3. EBSD inverse pole figure (IPF) maps show the grain morphologies of (a, d) Fe_{20}, (b, e) Fe_{15}, and (c, f) Fe_{10} HEAs after annealing at (a-c) 1173 K for 2.4×10^2 s (fine grain) and (d-f) 1373 K for 3.6×10^3 s (coarse grain). The samples in (a-c) with fine grains (hereinafter denoted by FG) were used for the *in-situ* neutron diffraction measurements.

observations, which are denoted as fine-grain (FG) samples.

To demonstrate the mechanical performance and clarify the effect of grain size, tensile tests of the HEAs were conducted at 293 K. Fig. 4 shows the engineering stress-strain curves of the Fe_{20} (Fig. 4a), Fe_{15} (Fig. 4b), and Fe_{10} (Fig. 4c) HEAs. Both the yield strength (σ_y) and ultimate tensile strength (σ_u) decreased with the increase in grain sizes in all three HEAs. The σ_y of fine-grain samples (6 μm) was 330.6 MPa (Fe_{20}), 366.9 MPa (Fe_{15}), and 432.7 MPa (Fe_{10}), but the σ_y decreased to 167.9, 188.3, and 222.0 MPa with the grain size increasing to 292, 211, and 205 μm. Meanwhile, the corresponding UTS decreased from 650, 804, and 889 MPa to 489, 640, and 690 MPa, respectively. However, both the σ_y and σ_u increased with the increase in Co and/or Cr content at the expense of Fe, Mn, and Ni. The tensile elongations of the Fe_{15} and Fe_{10} HEAs were larger than that of the Fe_{20} HEA. The elongation of the Fe_{20} samples ranged from 50.2 to 57.6%, with the grain size having an insignificant effect. However, the elongation changed from 60.5 to 90.1% in the Fe_{15} HEA and from 60.2 to 95.6% in the Fe_{10} HEA with the increase in the grain size, but the difference became negligible at the grain size larger than 70 μm.

The true strain–stress and strain-hardening curves for the three HEAs with grain sizes of ~ 6 μm and ~ 70 μm are presented in Fig. 4d–f. In the Fe_{20} HEA, the strain-hardening rate of the small-grain sample is larger than that of the large-grain sample at a small strain ($\varepsilon_t < 0.15$), but they become subequal at a large strain. For the Fe_{15} and Fe_{10} HEAs, the strain-hardening rates of the small-grain samples are higher than those of the large-grain samples at a small strain, but they decrease more rapidly than those of the large-grain samples. The strain-hardening rates of the large-grain samples decrease slowly, which results in a larger tensile elongation.

Fig. 5a depicts the relationship between the σ_y and the inverse square root of the grain size ($d^{-1/2}$) for the three HEAs, which follow a linear Hall–Petch relationship (Hall, 1951; Petch, 1953):

$$\sigma_y = \sigma_0 + \sigma_g = \sigma_0 + k_{H-P} d^{-1/2} \tag{5}$$

where σ_0 is the intrinsic yield strength without grain boundaries, σ_g is the contribution of grain boundaries to the yield strength, and k_{H-P} is the Hall–Petch coefficient. The fitted values of σ_0 are 131.8, 148.6, and 179.4 MP, and the k_{H-P} are 493.2, 531.3, and 610.6 MPa·μm$^{1/2}$ for the Fe_{20}, Fe_{15}, and Fe_{10} HEAs, respectively. This trend indicates that the friction stress for the dislocation motion in Fe_{10} is larger than those in Fe_{20} and Fe_{15} HEAs, and that grain refinement contributes more significantly to the increase in yield strength in Fe_{10} than in Fe_{20} and Fe_{15} HEAs. Fig. 5b shows the σ_u vs. d plot: a notable decrease in σ_u with the increase in d is observed at d smaller than 75 μm; at the same time, for coarser grains, σ_u decreases slowly with an increase in d.

We conducted *in situ* ND measurements to determine the plastic-deformation behavior. The *in situ* tensile stress-strain curves of the HEAs are shown in Fig. S1, where the measurement points are shown. During the ND profile collection, stress relaxation probably occurred because of the recovery of deformation-induced defects. Fig. 6 shows the ND profiles of the FG Fe_{20} (Fig. 6a), Fe_{15} (Fig. 6b), and Fe_{10} (Fig. 6c) HEAs at different strains. The diffraction peaks broadened with the increase in strain in all three HEAs. The Fe_{20} and Fe_{15} HEAs retained an FCC single-phase after tensile fracture at 293 K, whereas the HCP phase was formed after tensile deformation of the Fe_{10} HEA, as indicated in Fig. 6c. This trend means that the FCC → HCP phase transformation occurred.

Fig. 7 shows the lattice strain of the FG Fe_{20} (Fig. 7a), Fe_{15} (Fig. 7b), and Fe_{10} (Fig. 7c) HEAs, analyzed from the ND profiles, using

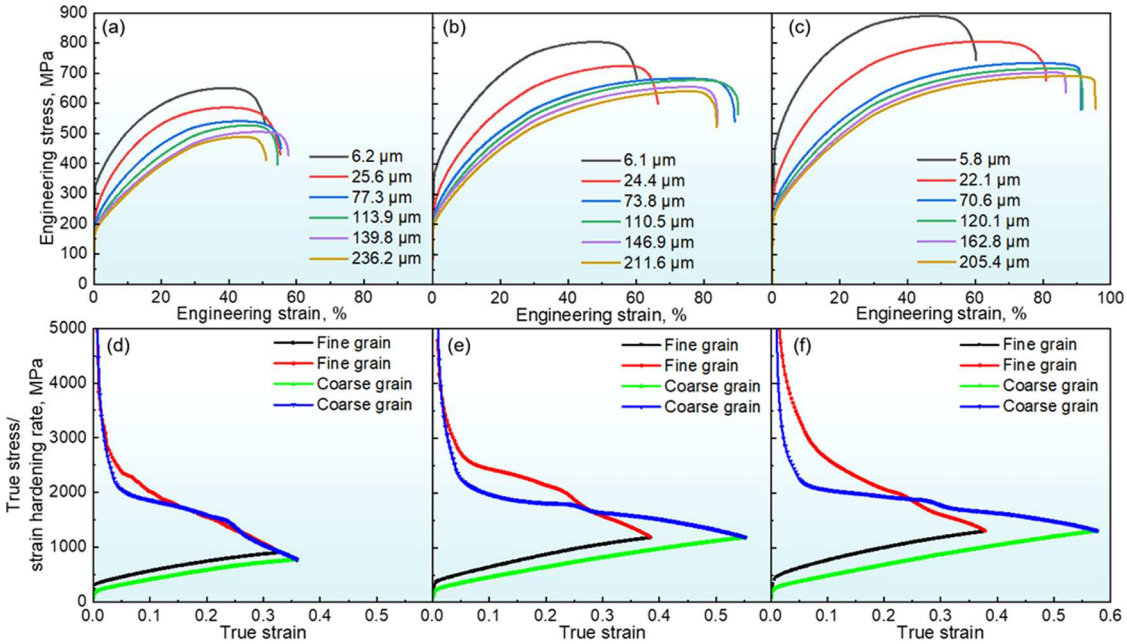

Fig. 4. (a-c) Room-temperature tensile engineering stress-strain curves of the (a) Fe_{20}, (b) Fe_{15}, and (c) Fe_{10} HEAs with different grain sizes. (d-f) True stress and strain hardening rate of the (d) Fe_{20}, (e) Fe_{15}, and (f) Fe_{10} HEAs with grain size of 5.8-6.2 μm and 70.6-77.3 μm.

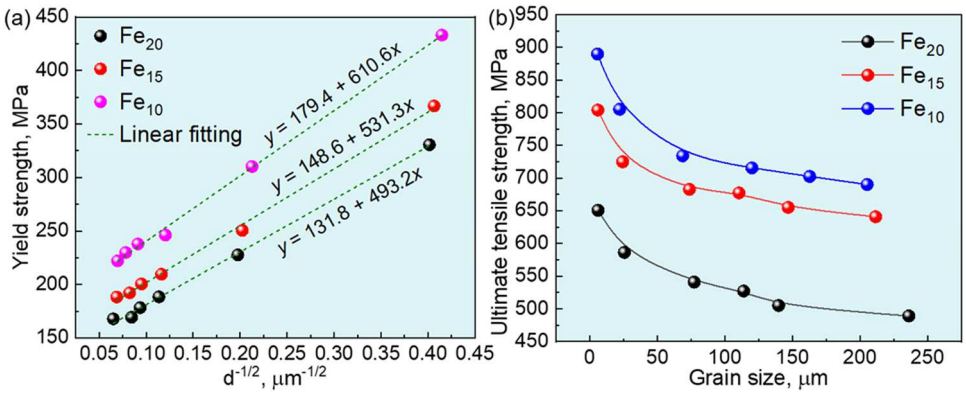

Fig. 5. (a) Yield strength v.s. square root of grain size and (b) ultimate tensile strength v.s. grain size acquired from the tensile tests of the Fe_{20}, Fe_{15}, and Fe_{10} HEAs.

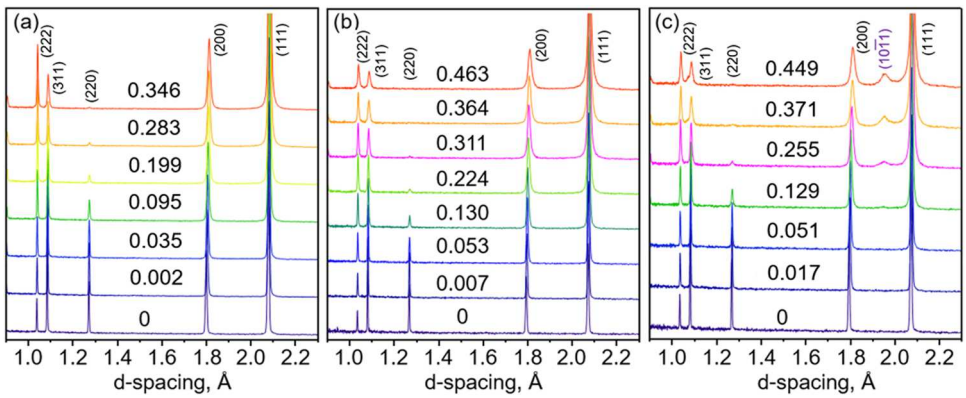

Fig. 6. In-situ neutron diffraction (ND) profiles of the FG Fe_{20} (a), Fe_{15} (b), and Fe_{10} (c) HEAs with grain size of ~6 μm before tensile and *in-situ* tensile deformed to various strains.

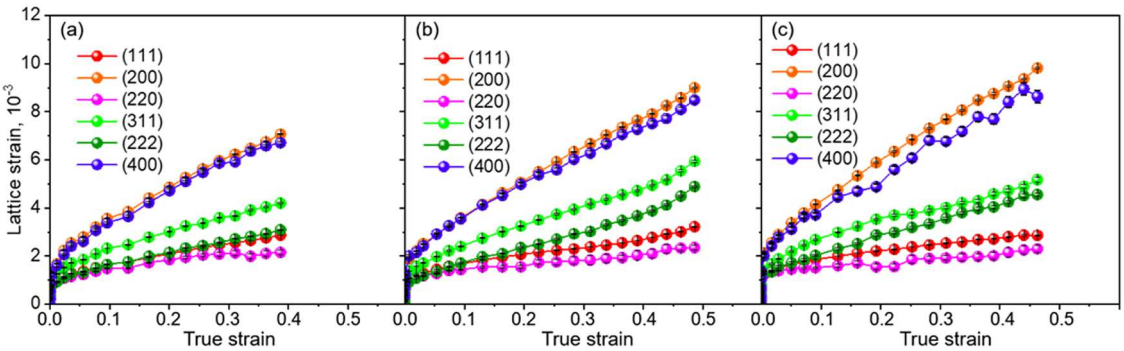

Fig. 7. Lattice strain of the FG Fe_{20} (a), Fe_{15} (b), and Fe_{10} (c) HEAs with grain size of ~6 μm at various tensile strains.

$$\varepsilon_{hkl} = \frac{d_{hkl} - d^0_{hkl}}{d^0_{hkl}} \tag{6}$$

where ε_{hkl} is the lattice strain of {*hkl*} planes, d_{hkl} is the lattice spacing of {*hkl*} planes at a given strain, d^0_{hkl} is the lattice spacing of {*hkl*} planes before the tensile test. It can be seen that the lattice strains of all the {111}, {200}, {220}, {311}, {222}, and {400} planes increase with the increase in tensile strains. The lattice strains follow the sequence of $\varepsilon_{220} < \varepsilon_{111} < \varepsilon_{222} < \varepsilon_{311} < \varepsilon_{400} < \varepsilon_{200}$, indicating that the <200> and <400> orientations are stiffer than the <220> and <111> orientations. In addition, the ε_{hkl} of the Fe_{10} HEA is larger than those of the Fe_{15} and Fe_{20} HEAs at an equivalent strain. It is worth noting that the difference between the ε_{111} and

ε_{222} of the Fe_{20} HEA is very small and does not change notably with the increase in the tensile strain. However, the corresponding difference is relatively large and increases with the increase in the strain in the Fe_{15} and Fe_{10} HEAs.

Table 1 shows the elastic moduli along the <111>, <200>, <220>, and <220> crystal orientations acquired from the linear fitting of the lattice strain and tensile stress in the elastic deformation regime. The elastic moduli exhibited anisotropic behavior. E_{111} and E_{220} are larger than E_{311} and E_{200}, indicating a higher stiffness along the <111> and <220> orientations. Furthermore, the elastic moduli follow the sequence of $Fe_{20} < Fe_{15} < Fe_{10}$. This trend is consistent with our previous reports that a decrease in Fe, Mn, and Ni and an increase in Co and Cr contents in HEAs increase Young's modulus. In addition, the lattice constant slightly decreases.

Based on the lattice strain, we acquired the stacking fault probability (P_{sf}), as follows (Frank et al., 2020a; Meric de Bellefon et al., 2018):

$$P_{sf} = \frac{32\pi}{3\sqrt{3}}\left(\frac{d_{222} - d_{222}^0}{d_{222}^0} - \frac{d_{111} - d_{111}^0}{d_{111}^0}\right) = \frac{32\pi}{3\sqrt{3}}(\varepsilon_{222} - \varepsilon_{111}) \tag{7}$$

The results are shown in Fig. 8a (Fe_{20}), 8b (Fe_{15}), and 8c (Fe_{10}). P_{sf} is very small in the Fe_{20} HEA, which reaches a maximum value of 4.25×10^{-3} at a strain of 0.398. However, the P_{sf} increases rapidly with the increase in strain in the Fe_{15} and Fe_{10} HEAs. The P_{sf} reaches 21.1×10^{-3} (Fe_{15}) and 31.7×10^{-3} (Fe_{10}), which is much larger than that of the Fe_{20} HEA, at a strain of ~ 0.4. Then, the P_{sf} increases to a maximum value of 32.3×10^{-3} (Fe_{15}) and 32.9×10^{-3} (Fe_{10}) at strains of 0.48 and 0.42, respectively. On the other hand, the twin fault (intrinsic SFs) probability acquired from the CMWP process is shown in Fig. 8d-f, where the values are comparable to that of the P_{sf}. This trend was also verified in CoCrFeNi HEA after deformation at various temperatures (Naeem et al., 2021). The large P_{sf} is correlated with the low intrinsic SFE (γ_{isf}) of the Fe_{15} and Fe_{10} HEAs, following a relationship described (Kang et al., 2012):

$$\gamma_{isf} = \frac{6.6a_0}{\pi\sqrt{3}}\left(\frac{2C_{44}}{C_{11} - C_{12}}\right)^{-0.37} \frac{<\xi_{50}^2>_{111}}{P_{sf}}\left(\frac{C_{44} + C_{11} - C_{12}}{3}\right) \tag{8}$$

where the $<\xi_{50}^2>_{111}$ is the mean-square microstrain obtained using Voigt approximation (Kang et al., 2012). The elastic constants of the single crystals were obtained from first-principles calculations, as shown in Table 2. The relationship between the $<\xi_{50}^2>_{111}$ and P_{sf} can be seen in Fig. S2. The obtained γ_{isf} values are also presented in Table 1. It can be seen that the γ_{isf} values are 11.6 and 7.8 mJ/m^2 for the Fe_{10} and Fe_{15} HEAs, respectively, which is much smaller than that for the Fe_{20} HEA (27 ~ 30 mJ/m^2) (Liu et al., 2018).

The square root of the dislocation density ($\rho^{1/2}$) in the three HEAs at different tensile strains is presented in Fig. 9. $\rho^{1/2}$ increases more rapidly with the increase in the strain in the Fe_{10} and Fe_{15} HEAs than in the Fe_{20} HEA. $\rho^{1/2}$ reaches a maximum value of 6.73×10^7 m^{-1} in the FG Fe_{20} HEA, but it is 10.3×10^7 and 14×10^7 m^{-1} in the Fe_{15} and Fe_{10} HEAs, respectively, at an equivalent strain. The dislocation density is correlated with the flow stress during tensile deformation, which will be discussed in Section 4.

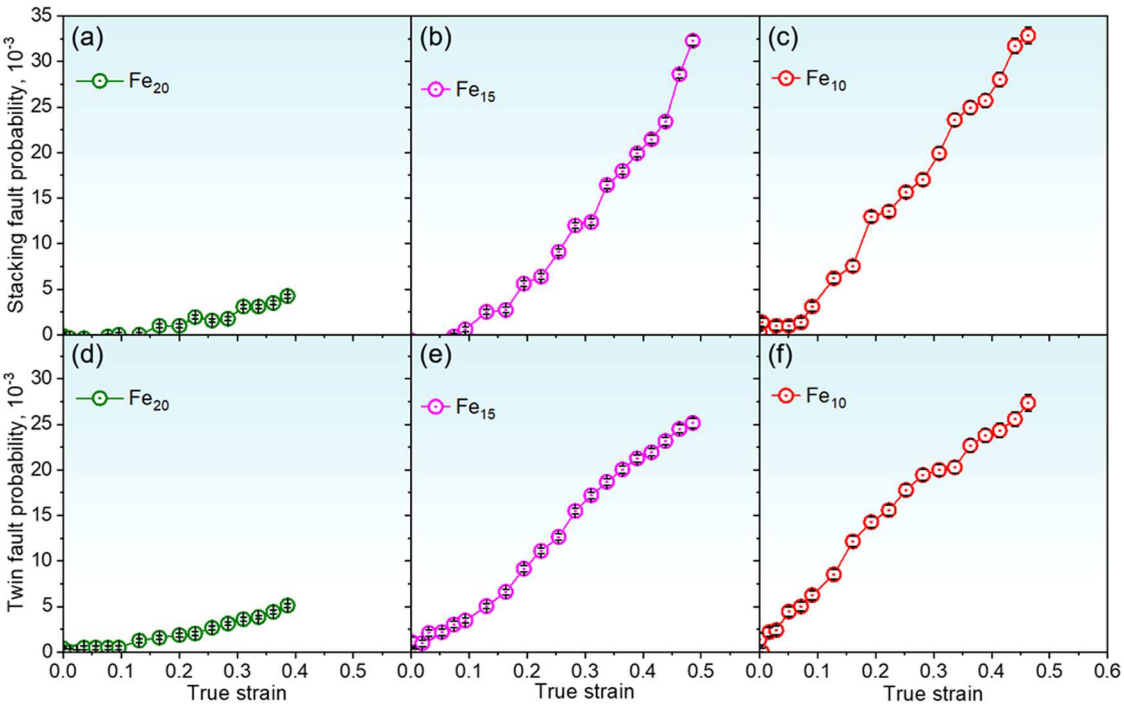

Fig. 8. (a-c) Stacking fault probability (P_{SF}) acquired from Eq. (7) and (d-f) twin fault probability acquired from the CMWP process of the FG Fe_{20} (a, d), Fe_{15} (b, e), and Fe_{10} (c, f) HEAs with grain size of ~6 μm at various tensile strains.

Table 2
Lattice parameter (a_0) and elastic constants (C_{11}, C_{12}, C_{44}) acquired from first-principle calculations at 0 K, and the shear modulus (G) experimentally measured by using a sing-around measurement technique at 298 K of the Fe_{20}, Fe_{15}, and Fe_{10} HEAs.

Sample	a_0 (nm)	C_{11} (GPa)	C_{12} (GPa)	C_{44} (GPa)	B (GPa)	G
Fe_{20}	0.3539	241.3	135.6	143.8	170.9	81 ± 0.5
Fe_{15}	0.3526	253.5	139.3	148.2	177.3	85 ± 0.5
Fe_{10}	0.3529	263.1	134.0	147.1	177.0	88 ± 0.5

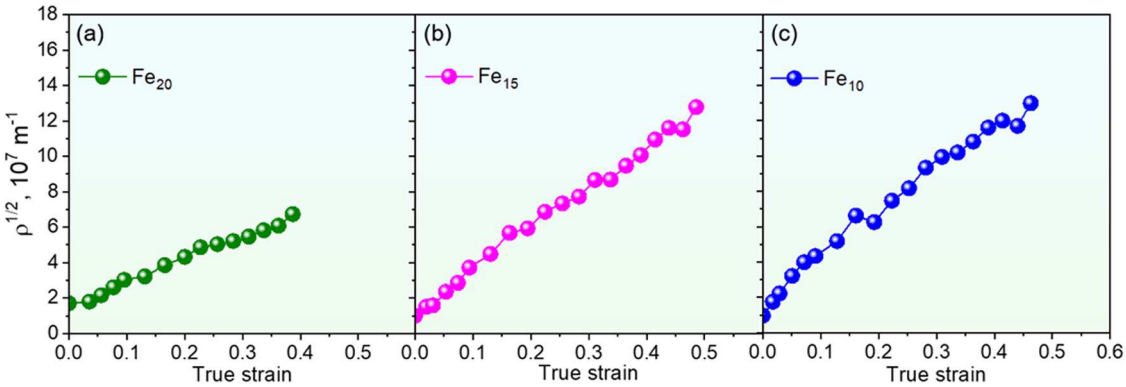

Fig. 9. Dislocation density of the FG Fe_{20} (a), Fe_{15} (b), and Fe_{10} (c) HEAs with grain size of ~6 μm *in-situ* tensile deformed to various strains.

Fig. 10 shows the evolution of the normalized peak intensity (I/I_0) in Fe_{20} (Fig. 10a), Fe_{15} (Fig. 10b), and Fe_{10} (Fig. 10c) HEAs. I/I_0 changes with the increase in strain: I/I_0 (220) decreases rapidly, but I/I_0 (111) and its second-order reflection, I/I_0 (222), increase. I/I_0 (200) and I/I_0 (400) slightly increase after tensile deformation, but I/I_0 (311) does not change significantly. The change in the peak intensity is attributed to the re-orientation of the grains during tensile deformation by either the grain rotation and/or mechanical twinning. The preferred slip system of the FCC-phase HEAs is {111} <110>. After yielding, (111) rotates towards the tensile axis, while (110) and its second-order reflection (220) rotate towards the direction parallel to the tensile axis, by which the dislocation slip becomes easier owing to the increase in the Schmid factor in the other three (111) variants.

The TEM observations were conducted to confirm the deformation of the substructures. The TEM bright-field images and selected area diffraction patterns in Figs. 11 and 12 exhibit the substructures of the Fe_{15} (Fig. 11) and Fe_{10} (Fig. 12) HEAs. In the Fe_{15} HEA, the SFs and dissociated dislocations (Fig. 11a) were observed at a relatively-small strain (6%). Nanotwins, SFs, and dislocation tangles were observed (Fig. 11b,e) at a strain of 15%. With an increase in the strain up to 30% (Fig. 11c,f), a high density of nano twins and their intersections were formed. In the Fe_{20} HEA, wavy dislocations were frequently observed at small strains, and mechanical twinning occurred at a strain of 25%. Meanwhile, the dislocation cell structures often formed at a large strain (Kaushik et al., 2021; Laplanche et al., 2016; Li et al., 2022; Otto et al., 2013). We can conclude that the plastic-deformation behavior and the evolution of the substructures are quite different, even though phase transformation was not detected in either HEA. At the same time, the Fe_{10} HEA exhibited a substructure similar to that of the Fe_{15} HEA at a strain of 6% (Fig. 12a,d), where SFs and dissociated dislocations were observed. However, the HCP-phase formed at a strain of 15% (Fig. 12b,e), which is different from the case of the Fe_{15} HEA. The HCP phase and FCC matrix follow an orientation relationship of $\{111\}_{FCC}//(0001)_{HCP}$, $<110>_{FCC}//[11\bar{2}0]_{HCP}$, which is in accordance with

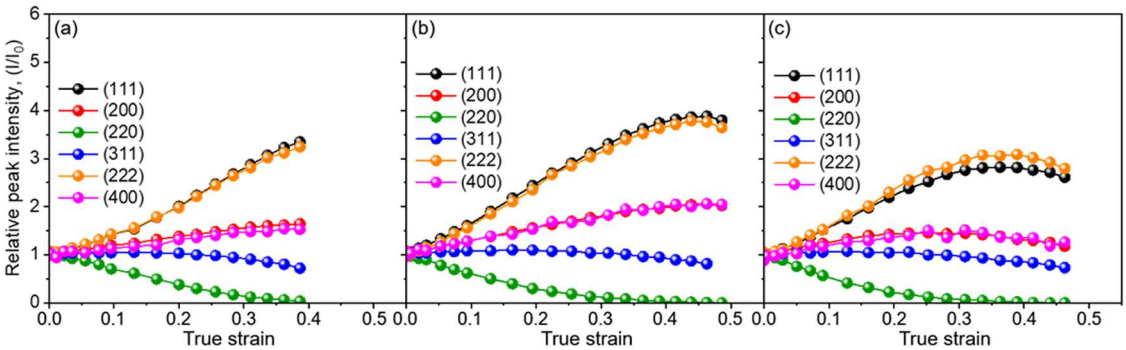

Fig. 10. Normalized peak intensity (I/I_0) evolution during *in-situ* tensile deformation of the FG Fe_{20} (a), Fe_{15} (b), and Fe_{10} (c) HEAs with grain size of ~6 μm before tensile and *in-situ* tensile deformed to various strain.

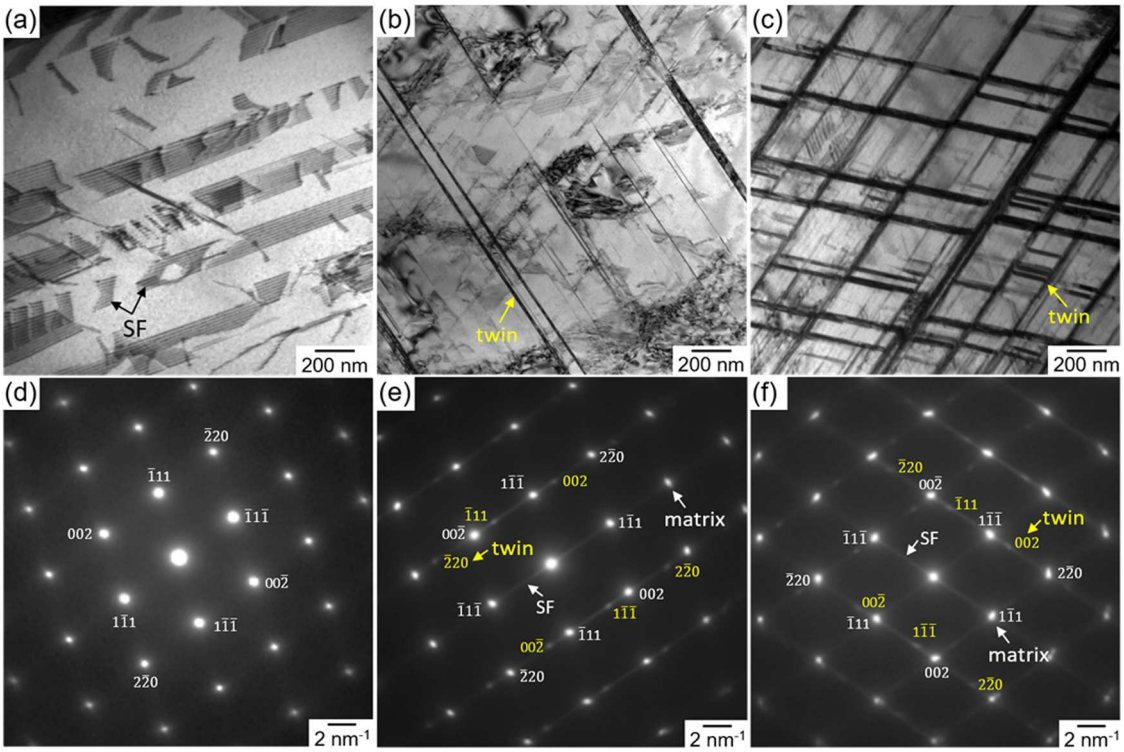

Fig. 11. (a-c) TEM bright-field images and (d-f) selected area diffraction patterns shows the substructures of the FG Fe_{15}-HEA after tensile to a strain of (a, d) 6%, (b, e) 15%, and (c, f) 30%. The images were acquired from the $[110]_{FCC}$ direction using a $g = (1\bar{1}\bar{1})$ vector.

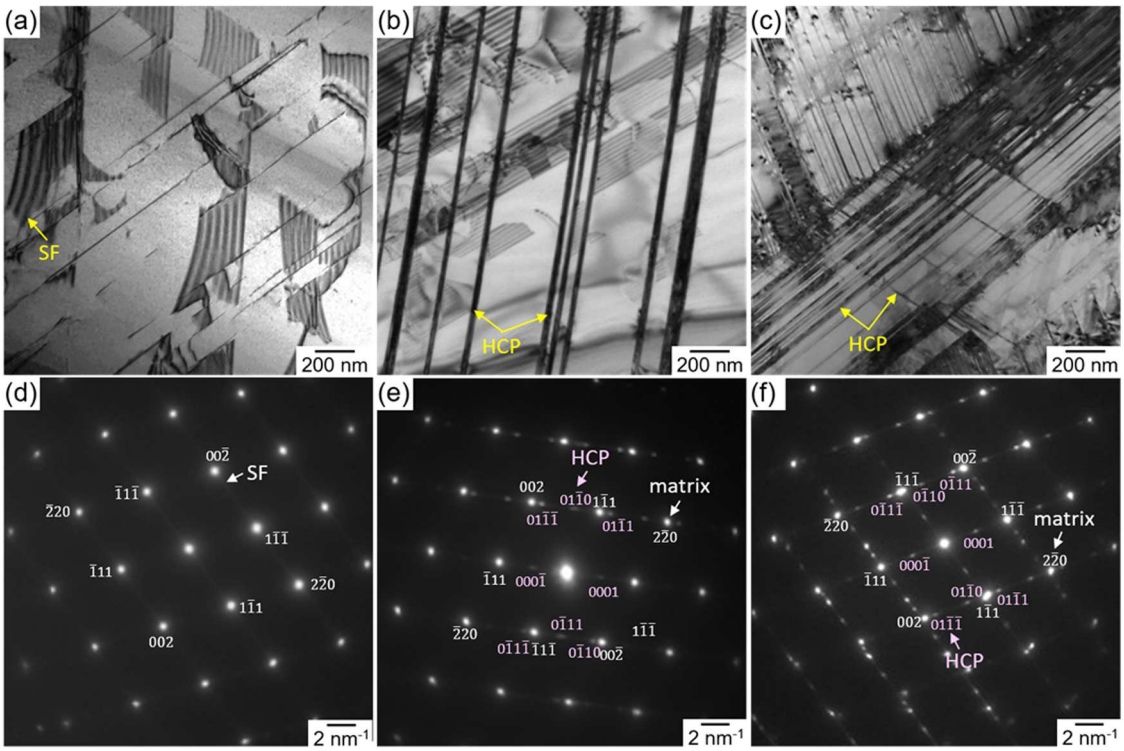

Fig. 12. (a-c) TEM bright-field images and (d-f) selected area diffraction patterns shows the substructures of FG Fe_{10}-HEA after tensile to a strain of (a, d) 6%, (b, e) 15%, and (c, f) 30%. The images were acquired from the $[110]_{FCC}$ direction using a $g = (1\bar{1}\bar{1})$ vector.

that reported for cobalt-based alloys and other FCC-phase TRIP HEAs. A large number of thin HCP-lamellae and their intersections were observed at a strain of 30% (Fig. 12c,f); dislocation tangles were also frequently observed at grain boundaries and the intersections of the HCP lamellae.

4. Discussion

4.1. Influence of composition and grain size on the yield strength of the HEAs

As shown in Fig. 5a, the σ_0 and k_{H-P} values of the three HEAs follow the order of $Fe_{20} < Fe_{15} < Fe_{10}$. The σ_0 is the intrinsic lattice friction stress equal to the critical flow stress of a single crystal oriented to multiple slips. The σ_0 of all the HEAs was much larger than those of pure Ni (14.2 MPa), pure Al (4.0 MPa), and Ni-40Co alloy (51.9 MPa). Local lattice distortion (LLD) and chemical undulation, or short-range order, were shown to increase the lattice friction force of HEAs (Labusch, 1970; Li et al., 2019; Okamoto et al., 2016; Toda-Caraballo and Rivera-Díaz-Del-Castillo, 2015; Varvenne et al., 2016). A solid-solution strengthening theory for the FCC-phase HEAs proposed that a great σ_0 is obtained by a large solute misfit parameter of δ and/or large shear modulus (G) (Varvenne et al., 2016), where δ is acquired by:

$$\delta = \left[\sum c_n\left(\Delta\overline{V}_n^2 + \sigma_{\Delta V_n}^2\right)\right]^{1/2} \tag{9}$$

Another model proved that the shear modulus and elastic mist were the prominent factors (Toda-Caraballo and Rivera-Díaz-Del-Castillo, 2015). Furthermore, it was proposed that the mean-square atomic displacement ($MSAD$) is a good scaling factor for predicting σ_0 (Okamoto et al., 2016).

The G and $\sqrt{MSAD}/b$ (b is the Burgers vector of dislocations) values for the three HEAs were evaluated by first-principles calculations. Here, ten SQS models were used for the average and standard deviation of $\sqrt{MSAD}$, and the results are presented in Fig. 13. The Co, Cr, Fe, Ni, and Mn atoms were displaced from their ideal positions in the crystal lattice. The magnitude of the displacement varied from element to element. The average values of the $\sqrt{MSAD}/b$ are 0.02188, 0.01918, and 0.02086 for the Fe_{20}, Fe_{15}, and Fe_{10} HEAs, respectively, revealing that the two Co-rich HEAs have a slightly-smaller LLD than the Fe_{20} HEA. However, the volume misfit of the five constituents did not exhibit significant differences between the three HEAs. The atomic volume of the fully-relaxed structure was also evaluated using Voronoi polyhedral technique. The atomic volume of the element, n (V_n), in the solid solution, is $V_{Co} = 11.12$ Å^3, $V_{Cr} = 12.27$ Å^3, $V_{Fe} = 12.09$ Å^3, $V_{Ni} = 10.94$ Å^3, and $V_{Mn} = 12.6$ Å^3 (Varvenne et al., 2016). The average atomic volume is $V_{av.} = \sum c_n V_n$, where c_n is the concentration of the element, n. The $V_{av.}$ are 11.804, 11.691, and 11.699 Å^3 for the Fe_{20}, Fe_{15}, and Fe_{10} HEAs, respectively. The solute misfit parameter δ is 1.21, 1.19, and 1.22 for the Fe_{20}, Fe_{15}, and Fe_{10} HEAs, respectively, indicating only negligible differences. Thus, the LLD and volume misfit cannot be used to interpret the large σ_0 values of the Fe_{15} and Fe_{10} HEAs. At the same time, the value of G increases from 81 GPa (Fe_{20}) to 85 GPa (Fe_{15}) and then to 88 GPa (Fe_{10}) as seen in Table 2. As σ_0 is linearly proportional to G, an increase in G contributes to an increase in σ_0. In addition, the modification of the chemical composition may tune the atomic short-range ordering behavior, meaning that ordering can enhance strength. These differences between the three HEAs require further investigation.

The k_{H-P} is 531.3 MPa·μm$^{1/2}$ and 610.6 MPa·μm$^{1/2}$ for the Fe_{15} and Fe_{10} HEAs, respectively, which are higher than 493.2 MPa·μm$^{1/2}$ for the Fe_{20} HEA (Fig. 5). k_{H-P} is much larger than those of pure Ni (180 MPa·μm$^{1/2}$), pure Al (43 MPa·μm$^{1/2}$), and dilute Ni-40Co alloy (181 MPa·μm$^{1/2}$) (Keller and Hug, 2008; Yoshida et al., 2017). It was verified that the value of k_{H-P} is affected by the LLD, SFE, and G (Yoshida et al., 2019, 2017): the factors hindering the movement of dislocations increase k_{H-P}. The LLD values of the HEAs are larger than those of pure metals and dilute alloys, contributing to the increase in k_{H-P}. Furthermore, k_{H-P} is correlated with G and γ_{isf} as follows (Shan Le Wang and Murr, 1980):

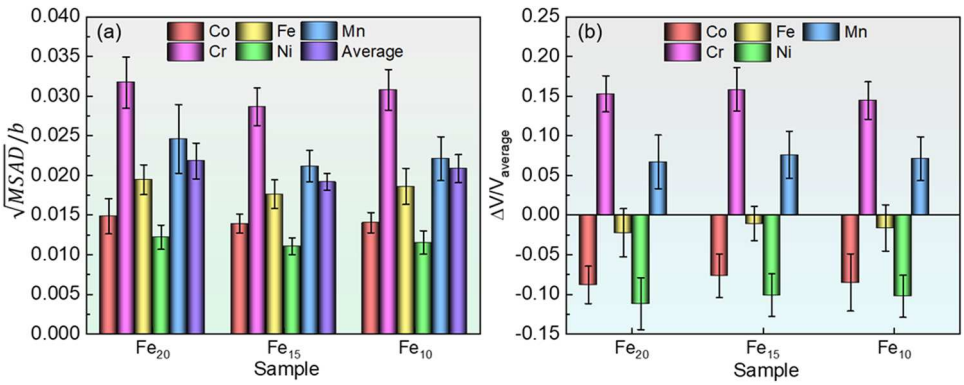

Fig. 13. (a) The $\sqrt{MSAD}/b$ of each elements and their average value and (b) the misfit volume (△V) divided by the average volume ($V_{average}$) of Co, Cr, Fe, Mn, Ni atoms in the Fe_{20}, Fe_{15}, and Fe_{10} HEAs.

$$k_{H-P} = \frac{Gb}{2\pi(1-\upsilon)}(\alpha - \delta\gamma_{isf}) \tag{10}$$

where υ is Poisson's ratio, and α and δ are dimensionally consistent constants. k_{H-P} increases with a decrease in γ_{isf} but also with an increase in G. Dislocation movement is activated by a shear stress when it reaches a critical value along the slip direction. Thus, a large G results in a greater friction resistance for the dislocation motion. Here, the increase in G contributes to the large k_{H-P} for the Fe_{15} and Fe_{10} HEAs, compared to the Fe_{20} HEA. At the same time, γ_{isf} affects the dislocation-slip behavior and the arrangement of dislocations, which is another reason for the differences in k_{H-P}. The polycrystalline structure yields when the stress concentration reaches a critical value in one grain, which is large enough to activate a new dislocation in adjacent grains. The stress concentration is generated from dislocation pile-ups, assisted by the cross slip of the dislocations (Cordero et al., 2016; Hansen, 2004). The local stress concentrations induced by a microscale dislocation pile-up also significantly contribute to the activation of the FCC→ HCP phase transformation and/or mechanical twinning in the HEAs (Peng et al., 2022). In the Fe_{15} and Fe_{10} HEAs with low SFE (Table 1), perfect dislocations are preferentially dissociated into a pair of Shockley partials by $\frac{a_0}{2}[10\bar{1}] \rightarrow \frac{a_0}{6}[2\bar{1}\bar{1}] + \frac{a_0}{6}[11\bar{2}]$, and one pair of Shockley partials bonds an SF, as shown in Figs. 11 and 12. The separation distance of the pair of Shockley partials is determined by SFE, where a smaller γ_{isf} results in a larger separation. The restriction of partials is a prerequisite for the cross-slip, which is suppressed by reducing SFE. Thus, a larger shear stress is required for dislocation pile-ups to reach the critical stress concentration. The decrease in SFE further contributes to the increase in k_{H-P}.

Based on the above analysis, we can conclude that grain-boundary strengthening is more prominent in the Co-rich HEAs, where grain refinement is more effective in increasing the yield strength of the HEAs than in pure metals, dilute alloys, and the equiatomic CoCrFeMnNi HEA.

4.2. Plastic-deformation mechanisms of the HEAs

The plastic-deformation mechanism of the Fe_{20} HEA was a wavy dislocation slip, forming dislocation tangles and mechanical twinning with an increase in the strain (Laplanche et al., 2016; Otto et al., 2013). In the Fe_{15} HEA, the dislocations were more likely to dissociate into Shockley partials-bonding SFs, and mechanical twinning occurred at a strain smaller than that in the Fe_{20} HEA. In contrast, in the Fe_{10} HEA, the plasticity mechanism was the stacking faulting and the FCC → HCP transformation. Different deformation behaviors are mainly attributed to the differences in SFE values. The formation of SFs by dissociating perfect dislocations is a prerequisite for both mechanical twinning and the FCC → HCP transformation (Byun, 2003; Fujita and Ueda, 1972; Idrissi et al., 2010; J.W. Brooks, M.H. Loretto, 1979; Narita and Takamura, 1974; Talonen and Hänninen, 2007; Venables, 1962). Overlapping the SFs in adjacent {111} planes generates local twins. However, overlapping SFs on every second {111} plane forms a local HCP structure (Byun, 2003; Fujita and Ueda, 1972; Idrissi et al., 2010; J.W. Brooks, M.H. Loretto, 1979; Narita and Takamura, 1974; Talonen and Hänninen, 2007; Venables, 1962). The twins or HCP plates then grew by successively overlapping the adjacent embryos, which formed hierarchical structures composed of abundant thin lamellae.

The differences between the Fe_{20} and Fe_{15} HEAs are discussed below. At γ_{isf} larger than the surface energy component (10 – 20 mJ/m^2 for steels) (Olson and Cohen, 1976; Talonen and Hänninen, 2007) of an SF, overlapping SFs on successive {111} planes are favorable. The separation distance (the width of the SFs) between the pairs of partial dislocations increased with an increase in the applied shear stress and diverged at the critical stress of γ_{isf}/b (Byun, 2003; Talonen and Hänninen, 2007). Thus, stable SFs are more easily formed with a decrease in γ_{isf}, and larger SFs can form in samples with lower SFE. The larger P_{sf} in Fig. 8b and the frequently-observed SFs in Fig. 11, demonstrate that stable SFs were more easily formed in the Fe_{15} HEA (γ_{isf}: 11.6 mJ/m^2) than in the Fe_{20} HEA (γ_{isf}: 27 – 30 mJ/m^2). At the same time, the onset of twinning requires a high-stress concentration, that is, critical twinning stress, through the multiplication of dislocations. The critical twinning stress is a linear or parabolic function of γ_{isf}, which decreases rapidly with a decrease in γ_{isf} (Byun, 2003; Talonen and Hänninen, 2007). In addition, the dynamic recovery of dislocations always proceeds with the accumulation of dislocations, which is impeded by the prevention of dislocations from the cross slip with a decrease in γ_{isf}. Based on the above two reasons, mechanical twinning is more preferentially activated in the Fe_{15} HEA than in the Fe_{20} HEA, which enhances strength and ductility.

In the Fe_{10} HEA, the γ_{isf} (7.8 mJ/m^2) is possibly smaller than the surface energy component, promoting the overlapping of SFs on every second {111} plane, which transforms the FCC crystal structure to the thermodynamically more stable HCP structure. Similar to the mechanical twinning, the widening of SFs diverges and forms stable HCP layers with a critical thickness under an applied shear stress. The critical shear stress and critical thickness of the HCP layers decreased with a decrease in γ_{isf} (Talonen and Hänninen, 2007). Thus, a large number of SFs (Figs. 8c and 12), as well as HCP lamellae (Fig. 12), were formed in the Fe_{10} HEA.

4.3. Strain-hardening mechanisms in the three HEAs

The tensile behaviors in Figs. 4 and 5 demonstrate that the flow stress increases with an increase in strain (strain hardening) in the HEAs, which is attributed to the multiplication of crystal defects (dislocations, SFs, nanotwins, and/or HCP lamellae). The flow stress can be described as:

$$\sigma = \sigma_0 + \sigma_g + \sigma_d + \sigma_x \tag{11}$$

where σ_d is the contribution of forest dislocations strengthening, and σ_x represents the other contributions such as SFs, twin, and/or HCP.

Strain hardening caused by forest dislocations can be expressed as follows (Kocks and Mecking, 2003; Lavrentev, 1980):

$$\sigma_d = \alpha MGb\left(\sqrt{\rho_d} - \sqrt{\rho_0}\right) \tag{12}$$

where α is a constant, and M is the average Taylor factor, ρ_0 and ρ_d represent the dislocation density before tensile and after tensile to a certain strain. The value of α ranges from 0.1 to 1.5 for FCC metals depending on the SFE, dislocation density, dislocation types, and the arrangement of dislocations (Lavrentev, 1980). Here, the value of α was acquired by linear fitting of the $(\sigma - \sigma_0 - \sigma_g)$ versus $MGb(\sqrt{\rho_d} - \sqrt{\rho_0})$ at a strain smaller than 15% enginnering strain. The calculated α value is 0.175, 0.12, and 0.103 for the Fe_{20}, Fe_{15}, and Fe_{10} HEAs, respectively. The M is affected by the texture of alloys, which has a value of 3.06 for an ideally non-texture polly-crystaline. The samples exhibit a relatively weak texture as seen in Fig. 3, therefore, the value of 3.06 is utilized for all the three HEAs in the present study.

The strain-hardening rate (θ) is proportional to $\frac{d\sigma}{d\varepsilon}$, i.e., $\frac{d\rho_d}{d\varepsilon}$. As seen in Fig. 4, θ of the HEAs follows $\theta_{Fe_{10}} > \theta_{Fe_{15}} > \theta_{Fe_{20}}$. In Fig. 9, the slopes of the curves represent $\frac{d\rho_d}{d\varepsilon}$, which is consistent with θ. The dislocations accumulated more rapidly in the Fe_{10} and Fe_{15} samples. During plastic deformation, the multiplication of dislocations and their dynamic recovery occurred simultaneously, where recovery is achieved by the cross-slip and annihilation of grouped dislocations with opposite signs (P. M. Anderson, J. P. Hirth, 2017). However, the dynamic recovery of dislocations in the Fe_{10} and Fe_{15} HEAs was suppressed by their low SFE, which impeded the constriction of partials needed for the cross-slip. In addition, the nano twins formed in the Fe_{20} and Fe_{15} HEAs as well as the HCP-bands formed in the Fe_{10} HEA contribute to enhancing the flow stress, denoted by σ_x, by the flowing two mechanisms: (i) The twin boundary and the FCC/HCP phase boundary acted as barriers to the motion of dislocations, thus reducing the mean free path of dislocations (Bouaziz and Guelton, 2001; Estrin and Mecking, 1984). This trend led to a more rapid multiplication of the dislocations. (ii) The formation of nanotwins or HCP lamellae reduced the average grain size, which increased the critical stress for the activation of macro-plastic deformation (Hall–Petch effect). All these factors contributed to the multiplication and storage of dislocations and resulted in the maintenance of a large strain-hardening ability to a very large strain and high stress. In addition, the SFs also contribute to hardening, as verified in Mg alloys, Cu-Al alloys, and TRIP-HEAs, where the SFs hinder the penetration of dislocations, analogous to other boundaries (Frank et al., 2020b; Jian et al., 2013a, 2013b; Pan et al., 2021; Tian et al., 2015). It was also indicated that an increase in the P_{sf} can enhance the flow stress.

The contributions of each item to the tensile flow stress were roughly estimated as shown in Fig. 14. The value of σ_d increases with the increase of strain in all three HEAs. But the σ_d value of the Fe_{15} and Fe_{10} HEAs is larger than that of the Fe_{20} HEA, attributed to the higher dislocation densities generated in the two low-SFE HEAs than that of the Fe_{20} HEA. Furthermore, the value of σ_x of the Fe_{15} and Fe_{10} HEAs is also larger than that of the Fe_{20} HEA. The possible reasons are as follows: (i) more SFs were formed in the Fe_{15} and Fe_{10} HEAs (Fig. 8) because of their low SFE, which contributes to increasing the flow stress by the SFs-strengthening; (ii) a large number of twin boundaries and/or FCC/HCP interfaces were formed in the Fe_{15} and Fe_{10} HEAs, which enhances the flow stress as discussed above. Based on all the above results and discussions, the differences in the tensile performance, plastic-deformation behavior, and strengthening mechanism among the three FCC-phase HEAs with different SFE were successfully clarified.

5. Conclusions

In this study, we investigated the room-temperature mechanical performance, plasticity behavior, and strain-hardening mechanisms of three representative FCC-phase HEAs with nominal compositions of $Co_{20}Cr_{20}Mn_{20}Ni_{20}Fe_{20}$ (Fe_{20}), $Co_{35}Cr_{20}Mn_{15}Ni_{15}Fe_{15}$ (Fe_{15}), and $Co_{35}Cr_{25}Mn_{15}Ni_{15}Fe_{10}$ (Fe_{10}) in at.%. This study provides deep insight into the mechanical performance, plasticity, and strengthening mechanisms of FCC-phase HEAs. Based on the results and discussion, the following conclusions can be drawn from this study.

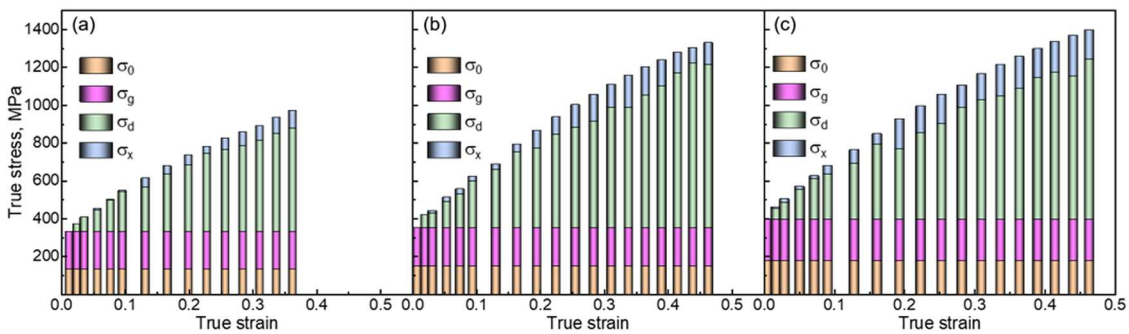

Fig. 14. Contribution of intrinsic lattice friction stress (σ_0), grain boundary strengthening (σ_g), forest dislocation strengthening (σ_d), and other strengthening mechanisms (σ_x) on the flow stress of the Fe_{20}, Fe_{15}, and Fe_{10} HEAs under various strains.

1 First, two Co-rich HEAs exhibited relatively slower grain-growth rates than the Fe_{20} HEA at high temperatures, and the mechanism warrants further investigations. The SFE of the Co-rich HEAs was 11.6 mJ/m^2 (Fe_{15}) and 7.8 mJ/m^2 (Fe_{10}), much smaller than that of the equiatomic Fe_{20} HEA (27-30 mJ/m^2). The increase in Co and/or Cr decreased the concentrations of Ni, Mn, and Fe, resulting in a decrease in the SFE.
2 The intrinsic yield strengths were 131.8 MPa (Fe_{20}), 148.6 MPa (Fe_{15}), and 179.4 MPa (Fe_{10}). The enhancement in the intrinsic yield strengths of Co-rich HEAs is mainly attributed to the large elastic modulus or elastic misfit, where the contribution from the local lattice distortion or solute volume misfit is small. The Hall–Petch coefficients of the HEAs were 493.2 MPa·μm$^{1/2}$ (Fe_{20}), 531.3 MPa·μm$^{1/2}$ (Fe_{15}), and 610.6 MPa·μm$^{1/2}$ (Fe_{10}), indicating that grain refinement is more effective for improving the yield strengths of the Co-rich HEAs.
3 The mechanism of plastic deformation in the Fe_{15} HEA was stacking faulting and mechanical twinning, which differed from the Fe_{20} HEA. A larger number of SFs and a higher density of dislocations formed in the Fe_{15} HEA than in the Fe_{20} HEA. Consequently, mechanical twinning was more easily activated. In contrast, stacking faulting and the FCC → HCP phase transformation occurred in the Fe_{10} HEA owing to its low SFE.
4 A high density of dislocations, a large number of SFs, and easily-formed nanotwins and/or HCP lamellae contributed to the promotion of the strain-hardening rate over a large strain, thus enhancing the strengths and ductility of the two Co-rich HEAs, compared to the Fe_{20} HEA. The grain size tended to have a more significant effect on the mechanical performance and strain-hardening behavior of HEAs with a decrease in SFE.

CRediT author statement

Daixiu Wei conceptualized the project, designed the research, conducted the experiments, and wrote the manuscript. **Daixiu Wei** was the leading research scientist of this work. **Wu Gong, Takuro Kawasaki, Stefanus Harjo**, and **Biao Cai** contributed to neutron diffraction experiments and analysis. **Tomohito Tsuru** conducted first-principle calculations. **Peter K. Liaw** contributed to discussion and revising manuscript. **Hidemi Kato** provided experimental facilities. All authors contributed to the discussion and revision of the paper.

Declaration of Competing Interest

The authors declare no conflict of interest.

Data Availability

Data will be made available on request.

Acknowledgments

D.W. was supported by the Grant-in-Aid for the Scientific Research from the Japan Society for the Promotion of Science (JSPS) KAKENHI (Grant No. 19K14838, 21K03766), and the Creation of Life Innovation Materials for Interdisciplinary and International Researcher Development' project. The current work is a cooperative program (Proposal No. 20G0420) of the Cooperative Research and Development Center for Advanced Materials, Institute for Materials Research, Tohoku University. The neutron-diffraction experiments were performed at BL19 in J-PARC with the proposals of 2020B0235. T.T. acknowledge the support of JST PRESTO Grant Number JPMJPR1998 and JSPS KAKENHI (Grant Numbers. JP19K04993, JP18H05453). The first-principles calculations were performed on the large-scale parallel computer system with SGI 8600 at JAEA. PKL very much appreciates the support of the U.S. Army Research Office Project (W911NF-13-1-0438 and W911NF-19-2-0049) with the program managers, Drs. M. P. Bakas, S. N. Mathaudhu, and D. M. Stepp and the support from the National Science Foundation (DMR-1611180 and 1809640) with the program directors, Drs. J. Yang, G. Shiflet, and D. Farkas.

Supplementary materials

Supplementary material associated with this article can be found, in the online version, at doi:10.1016/j.ijplas.2022.103417.

References

Agius, D., Kareer, A., Mamun, A.Al, Truman, C., Collins, D.M., Mostafavi, M., Knowles, D., 2022. A crystal plasticity model that accounts for grain size effects and slip system interactions on the deformation of austenitic stainless steels. Int. J. Plast. 152, 103249 https://doi.org/10.1016/j.ijplas.2022.103249.

Bahramyan, M., Mousavian, R.T., Brabazon, D., 2020. Study of the plastic deformation mechanism of TRIP-TWIP high entropy alloys at the atomic level. Int. J. Plast. 127, 102649 https://doi.org/10.1016/j.ijplas.2019.102649.

Beausir, B., Fressengeas, C., Gurao, N.P., Tóth, L.S., Suwas, S., 2009. Spatial correlation in grain misorientation distribution. Acta Mater. 57, 5382–5395. https://doi.org/10.1016/j.actamat.2009.07.035.

Beer Jr., Johnston, Dewolf, M., 2006. Mechanics of Materials, 5th editio. ed. BROOKS COLE PUBLISHING CO, McGraw Hill.
Borbély, A., Dragomir-Cernatescu, J., Ribárik, G., Ungár, T., 2003. Computer program ANIZC for the calculation of diffraction contrast factors of dislocations in elastically anisotropic cubic, hexagonal and trigonal crystals. J. Appl. Crystallogr. 36, 160–162. https://doi.org/10.1107/S0021889802021581.
Bouaziz, O., Guelton, N., 2001. Modelling of TWIP effect on work-hardening. Mater. Sci. Eng. A 319–321, 246–249. https://doi.org/10.1016/S0921-5093(00)02019-0.
Byun, T.S., 2003. On the stress dependence of partial dislocation separation and deformation microstructure in austenitic stainless steels. Acta Mater. 51, 3063–3071. https://doi.org/10.1016/S1359-6454(03)00117-4.
Cantor, B., Chang, I.T.H., Knight, P., Vincent, A.J.B., 2004. Microstructural development in equiatomic multicomponent alloys. Mater. Sci. Eng. A 375–377, 213–218. https://doi.org/10.1016/j.msea.2003.10.257.
Carter, C.B., Holmes, S.M., 1977. The stacking-fault energy of nickel. Philos. Mag. 35, 1161–1171. https://doi.org/10.1080/14786437708232942.
Connolly, D.S., Kohar, C.P., Inal, K., 2022. A novel crystal plasticity model incorporating transformation induced plasticity for a wide range of strain rates and temperatures. Int. J. Plast. 152, 103188 https://doi.org/10.1016/j.ijplas.2021.103188.
Cordero, Z.C., Knight, B.E., Schuh, C.A., 2016. Six decades of the Hall – Petch effect – a survey of grain-size strengthening studies on pure metals. Int. Mater. Rev. 61, 495–512. https://doi.org/10.1080/09506608.2016.1191808.
De Cooman, B.C., Estrin, Y., Kim, S.K., 2018. Twinning-induced plasticity (TWIP) steels. Acta Mater. 142, 283–362. https://doi.org/10.1016/j.actamat.2017.06.046.
Deng, Y., Tasan, C.C., Pradeep, K.G., Springer, H., Kostka, A., Raabe, D., 2015. Design of a twinning-induced plasticity high entropy alloy. Acta Mater. 94, 124–133. https://doi.org/10.1016/j.actamat.2015.04.014.
Estrin, Y., Mecking, H., 1984. A unified phenomenological description of work hardening and creep based on one-parameter models. Acta Metall. 32, 57–70. https://doi.org/10.1016/0001-6160(84)90202-5.
Fang, Q., Chen, Y., Li, J., Jiang, C., Liu, B., Liu, Y., Liaw, P.K., 2019. Probing the phase transformation and dislocation evolution in dual-phase high-entropy alloys. Int. J. Plast. 114, 161–173. https://doi.org/10.1016/j.ijplas.2018.10.014.
Fischer, F.D., Reisner, G., Werner, E., Tanaka, K., Cailletaud, G., Antretter, T., 2000. New view on transformation induced plasticity (TRIP). Int. J. Plast. 16, 723–748. https://doi.org/10.1016/S0749-6419(99)00078-9.
Frank, M., Chen, Y., Nene, S.S., Sinha, S., Liu, K., An, K., Mishra, R.S., 2020a. Investigating the deformation mechanisms of a highly metastable high entropy alloy using in-situ neutron diffraction. Mater. Today Commun. 23 https://doi.org/10.1016/j.mtcomm.2019.100858.
Frank, M., Nene, S.S., Chen, Y., Gwalani, B., Kautz, E.J., Devaraj, A., An, K., Mishra, R.S., 2020b. Correlating work hardening with co-activation of stacking fault strengthening and transformation in a high entropy alloy using in-situ neutron diffraction. Sci. Rep. 10, 1–10. https://doi.org/10.1038/s41598-020-79492-8.
Fujita, H., Ueda, S., 1972. Stacking faults and f.c.c. (γ) → h.c.p. (ϵ) transformation in 18 8-type stainless steel. Acta Metall. 20, 759–767. https://doi.org/10.1016/0001-6160(72)90104-6.
Gali, A., George, E.P., 2013. Tensile properties of high- and medium-entropy alloys. Intermetallics 39, 74–78. https://doi.org/10.1016/j.intermet.2013.03.018.
Gao, M.C., Zhang, B., Guo, S.M., Qiao, J.W., Hawk, J.A., 2015. High-Entropy Alloys in Hexagonal Close-Packed Structure. Metall. Mater. Trans. A 47, 3322–3332. https://doi.org/10.1007/s11661-015-3091-1.
Gludovatz, B., Hohenwarter, A., Catoor, D., Chang, E.H., George, E.P., Ritchie, R.O., 2014. A fracture-resistant high-entropy alloy for cryogenic applications. Science 345, 1153–1158. https://doi.org/10.1126/science.1254581, 80-.
Grässel, O., Frommeyer, G., 1998. Effect of martensitic phase transformation and deformation twinning on mechanical properties of Fe – Mn – Si – AI steels of Fe-Mn-Si-AI steels. Mater. Sci. Technol. 14 (12), 1213–1217. https://doi.org/10.1179/mst.1998.14.12.1213.
Gubicza, J., 2014. X-ray line profile analysis in materials science, X-Ray Line Profile Analysis in Materials Science. IGI Global, Hershey PA, USA. https://doi.org/10.4018/978-1-4666-5852-3.
Hall, E.O., 1951. The deformation and ageing of mild steel: II Characteristics of the Lüders deformation. Proc. Phys. Soc. Sect. B 64, 742–747. https://doi.org/10.1088/0370-1301/64/9/302.
Hansen, N., 2004. Hall – Petch relation and boundary strengthening. Scripta Mater. 51, 801–806. https://doi.org/10.1016/j.scriptamat.2004.06.002.
Hammert, B., Jacobsent, K.W., Milmanf, V., Payne, M.C., 1992. Stacking fault energies in aluminium. J. Phys. Condens. Matter. 4, 10453–10460. http://iopscience.iop.org/0953-8984/4/50/033.
Harjo, S., Ito, T., Aizawa, K., Arima, H., Abe, J., Moriai, A., Iwahashi, T., Kamiyama, T., 2011. Current Status of Engineering Materials Diffractometer at J-PARC. Mater. Sci. Forum 681, 443–448. https://doi.org/10.4028/www.scientific.net/MSF.681.443.
He, F., Wang, C., Han, B., Yeli, G., Lin, X., Wang, Z., Wang, L., Kai, J., 2022. Deformation faulting and dislocation-cell refinement in a selective laser melted 316L stainless steel. Int. J. Plast. 156, 103346 https://doi.org/10.1016/j.ijplas.2022.103346.
He, F., Yang, Z., Liu, S., Chen, D., Lin, W., Yang, T., Wei, D., Wang, Z., Wang, J., Kai, J.jung, 2021. Strain partitioning enables excellent tensile ductility in precipitated heterogeneous high-entropy alloys with gigapascal yield strength. Int. J. Plast. 144, 103022 https://doi.org/10.1016/j.ijplas.2021.103022.
He, Z., Jia, N., Yan, H., Shen, Y., Zhu, M., Guan, X., Zhao, X., Jin, S., Sha, G., Zhu, Y., Liu, C.T., 2021. Multi-heterostructure and mechanical properties of N-doped FeMnCoCr high entropy alloy. Int. J. Plast. 139 https://doi.org/10.1016/j.ijplas.2021.102965.
Homayounfard, M., Ganjiani, M., 2022. A large deformation constitutive model for plastic strain-induced phase transformation of stainless steels at cryogenic temperatures. Int. J. Plast. 156, 103344 https://doi.org/10.1016/j.ijplas.2022.103344.
Hu, K., Wu, M., Hinokuma, S., Ohto, T., Wakisaka, M., Fujita, J.I., Ito, Y., 2019. Boosting electrochemical water splitting: via ternary NiMoCo hybrid nanowire arrays. J. Mater. Chem. A 7, 2156–2164. https://doi.org/10.1039/c8ta11250a.
Huang, C., Elkhodary, K.I., Tang, S., 2019. Resolving the diffusionless transformation process of twinning in single crystal plasticity theory. Int. J. Plast. 120, 220–247. https://doi.org/10.1016/j.ijplas.2019.04.001.
Huang, S., Li, W., Lu, S., Tian, F., Shen, J., Holmström, E., Vitos, L., 2015. Temperature dependent stacking fault energy of FeCrCoNiMn high entropy alloy. Scr. Mater. 108, 44–47. https://doi.org/10.1016/j.scriptamat.2015.05.041.
Idrissi, H., Renard, K., Ryelandt, L., Schryvers, D., Jacques, P.J., 2010. On the mechanism of twin formation in Fe-Mn-C TWIP steels. Acta Mater. 58, 2464–2476. https://doi.org/10.1016/j.actamat.2009.12.032.
Brooks, J.W., Loretto, M.H., S, R.E., 1979. of martenstte nuclei in stainless steel. Acta Met. 27, 1839–1847.
Jian, W.W., Cheng, G.M., Xu, W.Z., Koch, C.C., Wang, Q.D., Zhu, Y.T., Mathaudhu, S.N., 2013a. Physics and model of strengthening by parallel stacking faults. Appl. Phys. Lett. 103 https://doi.org/10.1063/1.4822323.
Jian, W.W., Cheng, G.M., Xu, W.Z., Yuan, H., Tsai, M.H., Wang, Q.D., Koch, C.C., Zhu, Y.T., Mathaudhu, S.N., 2013b. Ultrastrong Mg alloy via nano-spaced stacking faults. Mater. Res. Lett. 1, 61–66. https://doi.org/10.1080/21663831.2013.765927.
Kang, M., Woo, W., Lee, Y.K., Seong, B.S., 2012. Neutron diffraction analysis of stacking fault energy in Fe-18Mn-2Al-0.6C twinning-induced plasticity steels. Mater. Lett. 76, 93–95. https://doi.org/10.1016/j.matlet.2012.02.075.
Kaushik, L., Kim, M.S., Singh, J., Kang, J.H., Heo, Y.U., Suh, J.Y., Choi, S.H., 2021. Deformation mechanisms and texture evolution in high entropy alloy during cold rolling. Int. J. Plast. 141, 102989 https://doi.org/10.1016/j.ijplas.2021.102989.
Keller, C., Hug, E., 2008. Hall – Petch behaviour of Ni polycrystals with a few grains per thickness. Mater. Lett. 62, 1718–1720. https://doi.org/10.1016/j.matlet.2007.09.069.
Kim, J.K., Kim, J.H., Park, H., Kim, J.S., Yang, G., Kim, R., Song, T., Suh, D.W., Kim, J., 2022. Temperature-dependent universal dislocation structures and transition of plasticity enhancing mechanisms of the Fe40Mn40Co10Cr10 high entropy alloy. Int. J. Plast. 148, 103148 https://doi.org/10.1016/j.ijplas.2021.103148.
Kocks, U.F., Mecking, H., 2003. Physics and phenomenology of strain. pdf Prog. Mater. Sci. 48, 171–273. https://doi.org/10.4324/9781315279015.
Kresse, G., Furthmüller, J., 1996. Efficient iterative schemes for ab initio total-energy calculations using a plane-wave basis set. Phys. Rev. B - Condens. Matter Mater. Phys. 54, 11169–11186. https://doi.org/10.1103/PhysRevB.54.11169.
Kresse, G., Hafner, J., 1993. Ab initio molecular dynamics for liquid metals. Phys. Rev. B 47, 558–561. https://doi.org/10.1103/PhysRevB.47.558.

Kresse, G., Joubert, D., 1999. From ultrasoft pseudopotentials to the projector augmented-wave method. Phys. Rev. B 59, 1758–1775. https://doi.org/10.1103/PhysRevB.59.1758.
Labusch, R., 1970. A Statistical Theory of Solid Solution Hardening. Phys. Status Solidi 41, 659–669. https://doi.org/10.1002/pssb.19700410221.
Lai, Q., Yang, H., Wei, Y., Zhou, H., Xiao, L., Ying, H., Lan, S., You, Z., Kou, Z., Feng, T., Lu, Q., Jacques, P., Pardoen, T., 2022. Transformation plasticity in high strength, ductile ultrafine-grained FeMn alloy processed by heavy ausforming. Int. J. Plast. 148 https://doi.org/10.1016/j.ijplas.2021.103151.
Laplanche, G., Kostka, A., Horst, O.M., Eggeler, G., George, E.P., 2016. Microstructure evolution and critical stress for twinning in the CrMnFeCoNi high-entropy alloy. Acta Mater 118, 152–163. https://doi.org/10.1016/j.actamat.2016.07.038.
Lavrentev, F.F., 1980. The Type of Dislocation Interaction as the Factor Determining Work Hardening. Mater. Sci. Eng. 46, 191–208. https://doi.org/10.1016/0025-5416(80)90175-5.
Li, L., Chen, Z., Kuroiwa, S., Ito, M., Kishida, K., Inui, H., George, E.P., 2022. Tensile and compressive plastic deformation behavior of medium-entropy Cr-Co-Ni single crystals from cryogenic to elevated temperatures. Int. J. Plast. 148 https://doi.org/10.1016/j.ijplas.2021.103144.
Li, Q.J., Sheng, H., Ma, E., 2019. Strengthening in multi-principal element alloys with local-chemical-order roughened dislocation pathways. Nat. Commun. 10, 1–11. https://doi.org/10.1038/s41467-019-11464-7.
Li, Y.Z., Liang, Z.Y., Huang, M.X., 2022. Strengthening contributions of dislocations and twins in warm-rolled TWIP steels. Int. J. Plast. 150 https://doi.org/10.1016/j.ijplas.2021.103198.
Li, Z., Pradeep, K.G., Deng, Y., Raabe, D., Tasan, C.C., 2016. Metastable high-entropy dual-phase alloys overcome the strength-ductility trade-off. Nature 534, 227–230. https://doi.org/10.1038/nature17981.
Liu, L., Zhang, Y., Li, J., Fan, M., Wang, X., Wu, G., Yang, Z., Luan, J., Jiao, Z., Liu, C.T., Liaw, P.K., Zhang, Z., 2022. Enhanced strength-ductility synergy via novel bifunctional nano-precipitates in a high-entropy alloy. Int. J. Plast. 153, 103235 https://doi.org/10.1016/j.ijplas.2022.103235.
Liu, S.F., Wu, Y., Wang, H.T., He, J.Y., Liu, J.B., Chen, C.X., Liu, X.J., Wang, H., Lu, Z.P., 2018. Stacking fault energy of face-centered-cubic high entropy alloys. Intermetallics 93, 269–273. https://doi.org/10.1016/j.intermet.2017.10.004.
Meric de Bellefon, G., Gussev, M.N., Stoica, A.D., van Duysen, J.C., Sridharan, K., 2018. Examining the influence of stacking fault width on deformation twinning in an austenitic stainless steel. Scr. Mater. 157, 162–166. https://doi.org/10.1016/j.scriptamat.2018.08.012.
Miracle, D.B., Senkov, O.N., 2017. Acta Materialia A critical review of high entropy alloys and related concepts. Acta Mater. 122, 448–511. https://doi.org/10.1016/j.actamat.2016.08.081.
Naeem, M., He, H., Harjo, S., Kawasaki, T., Lin, W., Kai, J.J., Wu, Z., Lan, S., Wang, X.L., 2021. Temperature-dependent hardening contributions in CrFeCoNi high-entropy alloy. Acta Mater. 221, 117371 https://doi.org/10.1016/j.actamat.2021.117371.
Narita, N., Takamura, J., 1974. Deformation twinning in silver- and copper-alloy crystals. Philos. Mag. 29, 1001–1028. https://doi.org/10.1080/14786437408226586.
NIST, 2000. Lanthanum hexaboride powder line position and line shape standard for powder diffraction. Standard SRM 660a. National Institute of Standards and Technology, U.S. Department of Commerce, Gaithersburg, MD.
Oishi-Tomiyasu, R., Yonemura, M., Morishima, T., 2012. Application of matrix decomposition algorithms for singular matrices to the Pawley method in Z-Rietveld. J. Appl. Crystallogr. 45, 299–308. https://doi.org/10.1107/S0021889812003998.
Oishi, R., Yonemura, M., Nishimaki, Y., Torii, S., Hoshikawa, A., Ishigaki, T., Morishima, T., Mori, K., Kamiyama, T., 2009. Rietveld analysis software for J-PARC. Nucl. Instrum. Method. Phys. Res. Sect. A Accel. Spectrometers, Detect. Assoc. Equip. 600, 94–96. https://doi.org/10.1016/j.nima.2008.11.056.
Okamoto, N.L., Yuge, K., Tanaka, K., Inui, H., George, E.P., 2016. Atomic displacement in the CrMnFeCoNi high-entropy alloy - A scaling factor to predict solid solution strengthening. AIP Adv. 6 https://doi.org/10.1063/1.4971371.
Olson, G.B., Cohen, M., 1976. A General Mechanism of Martensitic Nucleation: Part I . General Concepts and the FCC HCP Transformation. Metall. Trans. A 7, 1897–1904.
Otto, F., Dlouhý, A., Somsen, C., Bei, H., Eggeler, G., George, E.P., 2013. The influences of temperature and microstructure on the tensile properties of a CoCrFeMnNi high-entropy alloy. Acta Mater. 61, 5743–5755. https://doi.org/10.1016/j.actamat.2013.06.018.
Anderson, P.M., Hirth, J.P., L, J., 2017. Theory of Dislocations, 3rd editio. ed. Cambridge Univ. Press, Cambridge, UK.
Pan, Q., Zhang, L., Feng, R., Lu, Q., An, K., Chuang, A.C., Poplawsky, J.D., Liaw, P.K., Lu, L., 2021. Gradient cell–structured high-entropy alloy with exceptional strength and ductility. Science (80-.) 374, 984–989. https://doi.org/10.1126/science.abj8114.
Peng, Y., Ji, R., Phan, T., Gao, W., Levitas, V.I., Xiong, L., 2022. An atomistic-to-microscale computational analysis of the dislocation pileup-induced local stresses near an interface in plastically deformed two-phase materials. Acta Mater. 226, 117663 https://doi.org/10.1016/j.actamat.2022.117663.
Perdew, J.P., Burke, K., Ernzerhof, M., 1996. Perdew, Burke, Ernzerhof - 1997 - Generalized Gradient Approximation Made Simple(2) 3865–3868.
Petch, N.J., 1953. The Cleavage Strength of Polycrystals. J. Iron Steel Inst. 174, 174.
Pineau, A., Matdriaux, C., 1976. Twinning and Strain-Induced F.C.C. -~ H.C.P. Transformation on the Mechanical Properties of C o - N i - C r - M o Alloys 26, 123–132.
Raju, K.S., Krishna, M.G., Padmanabhan, K.A., Muraleedharan, K., Gurao, N.P., Wilde, G., 2008. Grain size and grain boundary character distribution in ultra-fine grained (ECAP) nickel. Mater. Sci. Eng. A 491, 1–7. https://doi.org/10.1016/j.msea.2007.11.072.
Abbaschian, Reza, Abbaschian, Lara, Reed-Hill, R., obert, E., 2009. Physical Metallurgy Principles, 4th editio. ed. Cl-Engineering, Stamford.
Ribárik, G., Jóni, B., Ungár, T., 2020. The convolutional multiple whole profile (CMWP) fitting method, a global optimization procedure for microstructure determination. Crystals 10, 623. https://doi.org/10.3390/cryst10070623.
Ribárik, G., Ungár, T., Gubicza, J., 2001. MWP-fit: A program for multiple whole-profile fitting of diffraction peak profiles by ab initio theoretical functions. J. Appl. Crystallogr. 34, 669–676. https://doi.org/10.1107/S0021889801011451.
Hertzberg, Richard W., Vinci, Richard P., H, J.L., 2013. Deformation and Fracture Mechanics of Engineering Materials. John Wiley & Sons, Inc, Danvers.
Schneider, M., George, E.P., Manescau, T.J., Záležák, T., Hunfeld, J., Dlouhý, A., Eggeler, G., Laplanche, G., 2020. Analysis of strengthening due to grain boundaries and annealing twin boundaries in the CrCoNi medium-entropy alloy. Int. J. Plast. 124, 155–169. https://doi.org/10.1016/j.ijplas.2019.08.009.
Senkov, O.N., Wilks, G.B., Miracle, D.B., Chuang, C.P., Liaw, P.K., 2010. Intermetallics Refractory high-entropy alloys. Intermetallics 18, 1758–1765. https://doi.org/10.1016/j.intermet.2010.05.014.
Wang, Shan Le, Murr, L.E., 1980. Effect of prestrain and stacking-fault energy on the application of the hall-petch relation in fcc metals and alloys. Metallography 13, 203–224. https://doi.org/10.1016/0026-0800(80)90001-4.
Sun, Y.T., Kong, X., Wang, Z.B., 2022. Superior mechanical properties and deformation mechanisms of a 304 stainless steel plate with gradient nanostructure. Int. J. Plast. 155, 103336 https://doi.org/10.1016/j.ijplas.2022.103336.
Talonen, J., Hänninen, H., 2007. Formation of shear bands and strain-induced martensite during plastic deformation of metastable austenitic stainless steels. Acta Mater 55, 6108–6118. https://doi.org/10.1016/j.actamat.2007.07.015.
Tian, Y.Z., Zhao, L.J., Chen, S., Shibata, A., Zhang, Z.F., Tsuji, N., 2015. Significant contribution of stacking faults to the strain hardening behavior of Cu-15%Al alloy with different grain sizes. Sci. Rep. 5, 2–10. https://doi.org/10.1038/srep16707.
Toda-Caraballo, I., Rivera-Díaz-Del-Castillo, P.E.J., 2015. Modelling solid solution hardening in high entropy alloys. Acta Mater. 85, 14–23. https://doi.org/10.1016/j.actamat.2014.11.014.
Tsai, M.H., Yeh, J.W., 2014. High-entropy alloys: A critical review. Mater. Res. Lett. 2, 107–123. https://doi.org/10.1080/21663831.2014.912690.
Ungár, T., Balogh, L., Ribárik, G., 2010. Defect-related physical-profile-based X-ray and neutron line profile analysis. Metall. Mater. Trans. A Phys. Metall. Mater. Sci. 41, 1202–1209. https://doi.org/10.1007/s11661-009-9961-7.
Ungár, T., Gubicza, J., Ribárik, G., Borbély, A., 2001. Crystallite size distribution and dislocation structure determined by diffraction profile analysis: Principles and practical application to cubic and hexagonal crystals. J. Appl. Crystallogr. 34, 298–310. https://doi.org/10.1107/S0021889801003715.
Van de Walle, A., Asta, M., Ceder, G., 2002. The alloy theoretic automated toolkit: A user guide. Calphad Comput. Coupling Phase Diagrams Thermochem. 26, 539–553. https://doi.org/10.1016/S0364-5916(02)80006-2.

Varvenne, C., Luque, A., Curtin, W.A., 2016. Theory of strengthening in fcc high entropy alloys. Acta Mater. 118, 164–176. https://doi.org/10.1016/j.actamat.2016.07.040.

Venables, J.A., 1962. The martensite transformation in stainless steel. Philos. Mag. 7, 35–44. https://doi.org/10.1080/14786436208201856.

Wei, D., Anniyaer, A., Koizumi, Y., Aoyagi, K., Nagasako, M., Kato, H., Chiba, A., 2019a. On microstructural homogenization and mechanical properties optimization of biomedical Co-Cr-Mo alloy additively manufactured by using electron beam melting. Addit. Manuf. 28, 215–227. https://doi.org/10.1016/j.addma.2019.05.010.

Wei, D., Gong, W., Kawasaki, T., Harjo, S., Kato, H., 2022a. Regulation of strength and ductility of single-phase twinning-induced plasticity high-entropy alloys. Scr. Mater. 216, 114738 https://doi.org/10.1016/j.scriptamat.2022.114738.

Wei, D., Gong, W., Wang, L., Tang, B., Kawasaki, T., Harjo, S., Kato, H., 2022b. Strengthening of high-entropy alloys via modulation of cryo-pre-straining-induced defects. J. Mater. Sci. Technol. 129, 251–260. https://doi.org/10.1016/j.jmst.2022.04.055.

Wei, D., Li, X., Heng, W., Koizumi, Y., He, F., Choi, W.-M., Lee, B.-J., Kim, H.S., Kato, H., Chiba, A., 2019b. Novel Co-rich high entropy alloys with superior tensile properties. Mater. Res. Lett. 7 (2), 82–88. https://doi.org/10.1080/21663831.2018.1553803.

Wei, D., Li, X., Jiang, J., Heng, W., Koizumi, Y., Choi, W.-M., Lee, B.-J., Kim, H.S., Kato, H., Chiba, A., 2019c. Novel Co-rich high performance twinning-induced plasticity (TWIP) and transformation-induced plasticity (TRIP) high-entropy alloys. Scr. Mater. 165, 39–43. https://doi.org/10.1016/j.scriptamat.2019.02.018.

Wei, D., Li, X., Schönecker, S., Jiang, J., Choi, W.-M., Lee, B.-J., Kim, H.S., Chiba, A., Kato, H., 2019d. Development of strong and ductile metastable face-centered cubic single-phase high-entropy alloys. Acta Mater. 181, 318–330. https://doi.org/10.1016/j.actamat.2019.09.050.

Wei, D., Wang, L., Zhang, Y., Gong, W., Tsuru, T., Lobzenko, I., Jiang, J., Harjo, S., Kawasaki, T., Bae, J.W., Lu, W., Lu, Z., Hayasaka, Y., Kiguchi, T., Okamoto, N.L., Ichitsubo, T., Kim, H.S., Furuhara, T., Ma, E., Kato, H., 2022c. Metalloid substitution elevates simultaneously the strength and ductility of face-centered-cubic high-entropy alloys. Acta Mater. 225, 117571 https://doi.org/10.1016/j.actamat.2021.117571.

Wilkens, M., 1970. The determination of density and distribution of dislocations in deformed single crystals from broadened X-ray diffraction profiles. Phys. Status Solidi 2, 359–370. https://doi.org/10.1002/pssa.19700020224.

Ye, Z., Li, C., Zheng, M., Zhang, X., Yang, X., Gu, J., 2022. In situ EBSD/DIC-based investigation of deformation and fracture mechanism in FCC- and L12-structured FeCoNiV high-entropy alloys. Int. J. Plast. 152, 103247 https://doi.org/10.1016/j.ijplas.2022.103247.

Yeh, B.J., Chen, S., Lin, S., Gan, J., Chin, T., Shun, T., Tsau, C., 2004. Nanostructured high-entropy alloys with multiple principal elements : Novel alloy design concepts and outcomes. Adv. Eng. Mater. 6 (5), 299–303. https://doi.org/10.1002/adem.200300567.

Yoshida, S., Bhattacharjee, T., Bai, Y., Tsuji, N., 2017. Friction stress and Hall-Petch relationship in CoCrNi equi-atomic medium entropy alloy processed by severe plastic deformation and subsequent annealing. Scr. Mater. 134, 33–36. https://doi.org/10.1016/j.scriptamat.2017.02.042.

Yoshida, S., Ikeuchi, T., Bhattacharjee, T., Bai, Y., 2019. Acta Materialia Effect of elemental combination on friction stress and Hall-Petch relationship in face-centered cubic high /medium entropy alloys. Acta Mater. 171, 201–215. https://doi.org/10.1016/j.actamat.2019.04.017.

Zhang, H., Li, C., Yao, G., Shi, Y., Zhang, Y., 2022. Effect of annealing treatment on microstructure evolution and deformation behavior of 304 L stainless steel made by laser powder bed fusion. Int. J. Plast. 155, 103335 https://doi.org/10.1016/j.ijplas.2022.103335.

Zhang, J.Y., He, Q.F., Li, J., Yang, Y., 2021. Chemical fluctuation enabling strength-plasticity synergy in metastable single-phase high entropy alloy film with gigapascal yield strength. Int. J. Plast. 139 https://doi.org/10.1016/j.ijplas.2021.102951.

Zhang, T.W., Ma, S.G., Zhao, D., Wu, Y.C., Zhang, Y., Wang, Z.H., Qiao, J.W., 2020. Simultaneous enhancement of strength and ductility in a NiCoCrFe high-entropy alloy upon dynamic tension: Micromechanism and constitutive modeling. Int. J. Plast. 124, 226–246. https://doi.org/10.1016/j.ijplas.2019.08.013.

Zhang, Y., Ting, T., Tang, Z., Gao, M.C., Dahmen, K.A., Liaw, P.K., Ping, Z., 2014. Progress in Materials Science Microstructures and properties of high-entropy alloys. Prog. Mater. Sci. 61, 1–93. https://doi.org/10.1016/j.pmatsci.2013.10.001.